

https://dspace.org/

Feasibility and the facilitation of off-site treatment planning services at Charlotte Maxeke Johannesburg Academic Hospital

Otten, Joseph Johannes

2024
University of the Witwatersrand, Johannesburg
https://hdl.handle.net/10539/42168

Otten, Joseph Johannes . (2024). Feasibility and the facilitation of off-site treatment planning services at Charlotte Maxeke Johannesburg Academic Hospital [Master's dissertation, University of the Witwatersrand, Johannesburg]. WireDSpace.https://hdl.handle.net/10539/42168

Downloaded from a DSpace repository. https://dspace.org/



Feasibility and the facilitation of off-site treatment planning services at Charlotte Maxeke Johannesburg Academic Hospital

by

Joseph Johannes Otten

2399575

A Research Report submitted in partial fulfilment of the requirements for the degree

Master of Science

in

Medical Physics

in the Faculty of Science, University of the Witwatersrand, Johannesburg, South Africa

Supervisor: Dr. Sonwabile Ngcezu

June 10, 2024

Declaration

In the submission of this work, I agree that I have read the University's Academic Integrity Policy. I declare that all material in this Research Report is my work except where there is clear acknowledgement and reference to the work of others.



Joseph Johannes Otten

9 day of July 20 24

at Pretoria, Gauteng

Acknowledgements

I would like to extend my deepest gratitude to Dr. Sowabile Ngcezu, whose guidance, support, and expertise have been invaluable throughout the course of my research. Dr. Ngcezu's mentorship has not only shaped this work but has also profoundly influenced my professional growth and academic journey.

My sincere appreciation goes to the Medical Physics department at Charlotte Maxeke Johannesburg Academic Hospital. The opportunity to use the Linear Accelerators (Linacs) and the system installation at the institution played a crucial role in the success of this project. The cooperation and assistance provided by the hospital staff were instrumental in facilitating my research.

I am also grateful to Varian, particularly to Niall M^{c}Andrew, who spearheaded the off-site planning system that was essential for my project. His leadership and dedication to the project were pivotal to its success. My thanks also extend to Eduard Gershkevitsh for his invaluable assistance with beam modelling and beam data verification, and to Theo Nair for his expert remote planning and training of our staff. The support and expertise provided by these individuals have significantly contributed to achieving the objectives of my research.

This research would not have been possible without the contributions of each individual and organization mentioned above. I am profoundly thankful for their generosity, support, and belief in my work.

Nomenclature

CMJAH	Charlotte Maxeke Johannesburg Academic Hospital
OTPS	Off-site Treatment Planning Service
IMRT	Intensity Modulated Radiotherapy Treatment
VMAT	Volumetric Modulated Arc Therapy
TPS	Treatment Planning System
Linac	Medical Linear Accelerator
AAPM	American Association of Physicists in Medicine
PDD	Percent-Depth-Dose
OF	Output Factors
DLG	Dosimetric Leaf Gaps
MLC	Multi Leaf Collimator
IAEA	International Atomic Energy Agency
MV	Megavoltage
CT	Computed Tomography
RED	Relative electron density
HU	Hounsfield Units
FFF	Flattening filter free
FS	Field Size
SSD	Source to surface distance
DICOM	Digital Imaging and Communications in Medicine
MU	Monitor unit
X	X-ray
MC	Monte Carlo
$\mathbf{D_{ref}}$	Dose at a specific reference depth
R&V	Record and Verify system
DTA	Distance to Agreement
DD	Dose Difference
AI	Artificial Intelligence

Abstract

The report encapsulates the comprehensive commissioning and validation process undertaken to integrate the Varian Eclipse treatment planning system (TPS) with Elekta Versa HD™linear accelerators, enabling off-site treatment planning services (OTPS). The initiative aimed to enhance the efficiency of treatment planning and expand access to care. The process involved meticulous collection and modelling of beam data from four Versa HD™Linacs within the Eclipse system. Measurements were conducted to characterize the beam properties, including profiles, percent depth dose (PDD) curves, and output factors (OF). A pivotal aspect of the validation was the acquisition and verification of the computed tomography (CT) to electron density curve, which is crucial for accurate dose calculations. The Anisotropic Analytical Algorithm (AAA) was employed for dose calculations, with its accuracy confirmed through point dose measurements and gamma index comparisons. Fine-tuning of multi-leaf collimator (MLC) transmission and dosimetric leaf gap (DLG) parameters was achieved through iterative plan measurements and optimisations. The culmination of the validation process was the end-to-end testing, adhering to the International Atomic Energy Agency (IAEA) audit methodology, utilising CIRS phantoms (Clark et al., 2019). This testing was conducted on the clinical servers, with patient-specific quality assurance results exhibiting gamma pass rates above 90% for distance to agreement (DTA) of 3mm and a dose difference (DD) 3%, indicative of the system's accuracy. The study demonstrated the feasibility of remote treatment planning for Elekta Linacs using the Varian Eclipse TPS. The rigorous commissioning and validation process ensured the dosimetric accuracy and quality of the integrated system. The successful validation of the Eclipse TPS for clinical use suggests that this integration could significantly streamline the planning work, potentially alleviating treatment backlogs and enhancing the delivery of care in radiation therapy.

Contents

1 Introduction **10**

2 Theoretical Background **15**

2.1 Literature Review 15

2.2 Beam data library: Commissioning and Data collection 16

2.2.1 Machine-Specific Characteristics 18

2.2.2 Dosimetric measurements 19

2.2.3 Chamber volume correction 21

2.2.4 Multi leaf collimator (MLC) Transmission 21

2.2.5 Dosimetric leaf gaps (DLGs) 22

2.3 Verification of TPS features 23

2.3.1 Confirmation of Non-Dosimetric Aspects 23

2.3.2 Confirmation of Dosimetric Aspects 23

2.3.2.1 Calculation Checks 23

2.3.2.2 Algorithm Checks 27

2.3.2.3 Accuracy in advanced treatment techniques . . 28

2.3.3 CT to ED data 28

2.3.4 Auto contouring using AI. 30

2.3.5 Workflow for a radiation oncology department. 31

2.4 Linac Treatment Planning Modelling and Optimisation 33

2.4.1 Analytical Anisotropic Algorithm (AAA) 34

2.4.2 Beam Model Auto-Fitting Process 36

2.4.3 Gamma Index 37

3 Materials and Methods **40**

3.1 Commissioning materials and equipment 40

3.2 Beam data collection: PDDs, profiles and Output Factors (OFs) 42

3.3 MLC transmission and DLGs 46

3.4 Validation of the Eclipse TPS 47

3.4.1 CT-ED calibration curve 50

3.4.2 Verification of the AAA calculation model based on commissioning data. 50
3.4.3 MLC parameter fine-tuning 52
3.4.4 IAEA End-to-End methodology 53

4 Results and Discussion **57**
4.1 Commissioned beam data 57
4.2 CT to RED 63
4.3 Beam modelling in Eclipse 66
4.4 DLG measurements 71
4.5 Comprehensive Dosimetric Validation and Quality Assurance of Beam Models 72
4.6 Implementation and Challenges of a Collaborative Off-site Treatment Planning Services 81
4.6.1 Workflow Implemented 81
4.6.2 Test patients results 82
4.6.3 Feasibility of OTPS 84
4.6.4 Implementation Challenges 85
4.6.5 Future research 86

5 Conclusion **88**

References **90**

List of Figures

1 Typical workflow implemented in a radiation oncology department. 32

2 Illustration of the method used in the AAA algorithm (Mayles et al., 2022) 36

3 Illustrations of one-dimensional dose comparison analyses in scenarios with both shallow (a) and steep (b) dose gradients. The gamma value indicates how closely the evaluated distribution approximates the reference distribution. In mild dose gradients, the γ test primarily serves as a DD evaluation, whereas in pronounced dose gradients, it effectively measures the DTA. . . 38

4 CIRS Shane phantom depicting all elements. 49

5 CT scan of the SHANE phantom's shoulder region showing electron density plugs: (A) water, (B) cortical bone, (C) trabecular bone, (D) lung exhale, (E) lung inhale, (F) spinal cord, (G) soft tissue (Clark et al., 2019). 49

6 CIRS M062 phantom for CT to RED/Mass density conversion curve measurements scanned on a Canon Aquillion LB CT scanner. 51

7 RW3 slab phantom with an insert suitable for a PTW Semiflex 0.125 cc chamber at 5 cm depth scanned on a Canon Aquillion LB CT scanner. 52

8 CT examination of the CIRS Shane H&N phantom displaying the ion chamber channels' locations and their respective positions, depicted in (a) the transverse plane, (b) 3-D display, (c) sagittal view, and (d) coronal view (Kazantsev et al., 2020). . . 56

9 10X PDD for various FS using the PTW microDiamond 0.004 cc for FSs between $2 \times$ cm^2 - $4 \times 4\,$cm^2 and the PTW Semiflex 3D 0.07 cc (both chambers shown in Table 4) for FS between $5 \times 5\,$cm^2 - $40 \times 40\,$cm^2 and at an SSD of 90 cm. 58

10 10X inline and cross-line profiles for $3 \times 3\,cm^2$ FS at depths d_{max}, 5 cm, 10 cm, 20 cm and 30 cm using the PTW microDiamond 0.004 cc (shown in Table 4) at an SSD of 90 cm. 59
11 6X cross-plane and in-plane profiles of $1 \times 1\,cm^2$ FS scanned with PTW microDiamond 0.004 cc (shown in Table 4) at an SSD of 90 cm, depth 10 cm. 60
12 (a)Comparison of measured and AGL OFs for square FSs. (b) Difference between measured and AGL OF values. 62
13 (a)Comparison of CT to RED curves measured with CIRS M062 phantom and CIRS SHANE phantom for the Canon Aquillion LB CT scanner. (b) Difference between CIRS M062 phantom and CIRS SHANE phantom RED values. 65
14 (a) Comparison of measured and modelled profiles for 6X, $40 \times 40, cm^2$ at 1.5 cm depth, showing discrepancies. (b) Comparison of measured and modelled profiles for 6X, $35 \times 35, cm^2$ at 1.8 cm depth, showing discrepancies. (c) Comparison of measured and modelled profiles for 10X, $30 \times 30, cm^2$ at 1.5 cm depth, showing discrepancies. 67
15 (a) Comparison of measured and modelled percentage depth dose for 6X, $15 \times 15\,cm^2$, highlighting discrepancies. (b) Comparison of measured and modelled percentage depth dose for 6X FFF, $4 \times 4\,cm^2$, highlighting discrepancies. (c) Comparison of measured and modelled percentage depth dose for 10X, $10 \times 10\,cm^2$, highlighting discrepancies. 69
16 (a) Comparison of measured and modelled half diagonal profile for 6X beams at $40 \times 40\,cm^2$ FS. (b) Comparison of measured and modelled half diagonal profile for 6X FFF beams at $40 \times 40\,cm^2$ FS. (c) Comparison of measured and modelled half diagonal profile for 10X beams at $40 \times 40\,cm^2$ FS. 70

17 The measurement of DLG, using the sweeping-gap technique as a modelling factor for MLC leaf end transmission, reveals a linear relationship in the data. This analysis produced initial DLG values specific to each energy: 0.21 mm (6X), 0.22 mm (6X FFF), and 0.24 mm (10X). 72

18 Final Workflow implemented at CMJAH for OTPS provided by Niall M^{c}Andrew (Varian). 83

List of Tables

1 Example of Assessments to Validate Input of Anatomical Patient Data into TPS (Mayles et al., 2022) 24

2 Example of Evaluations for Anatomical Data Processing (Mayles et al., 2022). 25

3 Example of Evaluations for Representation of Beam Geometry (Mayles et al., 2022). 26

4 Detector Characteristics and Assigned Tasks for VersaHD Commissioning. 43

5 CIRS Shane phantom structure with corresponding volumes and TPS limits. 55

6 HU values obtained from scanning the CIRS M062 phantom with various RED inserts. 64

7 Measured DLG and MLC transmission. 71

8 Reference dosimetry results using an independent chamber. . . . 73

9 Comparison of initial measured and calculated doses using AAA algorithm on the test server for the four field plans (Beam parameters indicated below each energy) on a RW3 slab phantom. The results were normalised to a $10 \times 10\,\mathrm{cm}^2$ field delivering 1 Gy to isocentre at SSD=95 cm, depth 5 cm. 74

10 Point dose measurements in the RW3 slab phantom at the isocentre location for VMAT plans calculated using AAA algorithm on the test server. 75

11 DLG and MLC transmission values used in the beam model. . . 75

12 Comparison of initial measured and calculated doses using AAA algorithm for CIRS Shane phantom for 6X. 77

13 Comparison of initial measured and calculated doses using AAA algorithm for CIRS Shane phantom for 6X FFF. 78

14 Comparison of initial measured and calculated doses using AAA algorithm for CIRS Shane phantom for 10X. 79

15 Patient-Specific Quality Assurance results for each test plan with DTA of2mm and DD 5% 80
16 Patient-Specific Quality Assurance results for the five mock patients with DTA of 3 mm and DD 3% 84

1 Introduction

Radiotherapy stands as a cornerstone in cancer treatment, with around 50% of patients necessitating its use during their therapeutic journey (Khan and Gibbons, 2020). The essence of effective radiotherapy lies in the precise orchestration of treatment planning systems, which seek to optimize dose delivery to tumors while safeguarding adjacent healthy tissues (Chen, 2014). The urgency of addressing the growing cancer treatment backlog in Gauteng, South Africa, has become increasingly apparent, with a burgeoning number of patients awaiting access to external radiotherapy (Loh; Daily Maverick, 2024).

At Charlotte Maxeke Johannesburg Academic Hospital (CMJAH), the discrepancy between the number of patients treated in 2020 (2076), 2021 (1622), 2022 (2619), and 2023 (2086) underscores a pressing need to bolster patient outcomes and their quality of life as the wait list grows longer, with an estimated 2000 patients currently on the waiting list (Hanna et al., 2020). On average, each external beam therapy machine handles about 25-55 patients per day in public hospitals in South Africa (Tohyama et al., 2023), indicating the significant pressure on available resources. The prevailing target diagnosis-to-treatment time for radiotherapy patients in Gauteng is approximately 12-20 weeks, but this is often extended due to resource constraints.

While the advanced capabilities of Elekta Versa HD™ units (Elekta Instruments AB, Stockholm, Sweden, 2024) and Varian's Eclipse Treatment Planning System (TPS) (Varian Medical Systems, Palo Alto, CA, 2024) are recognized, the bottleneck in elevating patient throughput at CMJAH transcends technological constraints. A notable hurdle is the diminished output from treatment planning due to staffing shortages. The departure of skilled planning staff to the private sector not only depletes the hospital's service delivery but also significantly affects patient treatment outcomes (Duffton et al., 2020). The loss of experienced planners reduces the accuracy of treatment plans, delays the commencement of patient treatment, and increases the workload and stress on

remaining staff, potentially leading to errors. This delineates the complexity of the challenge, highlighting that augmenting technological infrastructure alone is insufficient.

This research introduces an innovative approach by suggesting the adoption of a remote treatment planning service to enhance the capabilities of the current workforce (Kisling et al., 2019). Far from intending to supplant local planning capabilities (which includes 10 Monaco 6.1.2.0 used by about 3-5 radiotherapy planners as of January 2024), this innovative approach is designed to enhance them, underscoring CMJAH's commitment to nurturing local expertise and ensuring a reliable treatment planning process. The proposed remote service is envisioned as a scalable solution, adaptable to the specific requirements of the hospital, thereby providing a sustainable model for increasing planning capabilities and patient throughput without the sole dependency on additional equipment.

This research proposes a paradigm shift by advocating for a remote treatment planning service that significantly deviates from traditional, on-site planning processes at CMJAH. Unlike conventional methods where treatment planning is conducted entirely within the hospital's premises by the local staff, the remote service model capitalizes on the expertise of off-site treatment planners. These planners, who are employed by Varian, must meet the stringent requirements outlined by the Health Professions Council of South Africa (HPCSA) to be authorized to access patient data and create treatment plans, ensuring compliance with local regulations and standards. This approach not only aims to alleviate the staffing constraints but also introduces an innovative collaboration model that leverages advanced technology and secure data transmission protocols to facilitate treatment planning from afar. The remote planning service operates through secure data exchange mechanisms, ensuring patient data integrity and compliance with local data protection regulations. By outsourcing some of the planning workload, CMJAH can effectively increase patient throughput without the immediate need for additional personnel or technol-

ogy upgrades. However, this model introduces new challenges, such as the necessity for rigorous data security measures, dependence on stable internet connectivity for seamless data transfer, and potential delays in communication across different time zones. Moreover, there's a critical need to ensure that the remote planning service integrates smoothly with CMJAH's existing treatment protocols and infrastructure, requiring initial setup and ongoing management to address any technical or operational issues that may arise. Despite these challenges, the remote treatment planning service stands as a promising solution to enhance the hospital's capacity to deliver timely and effective radiotherapy treatments, thus addressing the critical backlog of cancer care in Gauteng.

In exploring the feasibility of this integrated approach, the study will examine technical, logistical, and clinical facets, with a focus on seamlessly commissioning Elekta treatment data into the Eclipse system. Through this lens, the research report aims to illuminate the potential of such integration in refining radiotherapy treatment planning at CMJAH through the means of a 100 patient pilot study, contributing to the broader scientific discourse on optimising radiotherapy treatment delivery.

Research Questions, Hypothesis, and Objectives

This investigation is anchored by the following research questions:

- Can a remote treatment planning service effectively augment the existing treatment planning capabilities at CMJAH?
- What are the technical, logistical, and clinical challenges associated with integrating remote treatment planning with Elekta Versa HD™units and Varian Eclipse TPS, and how can these be overcome?

The underlying hypothesis posits that integrating a remote treatment planning service with CMJAH's current infrastructure will significantly enhance treatment planning efficiency, accuracy, and patient throughput, without compromising the development of local expertise.

Acknowledging the complexities and challenges delineated earlier, this research aims to bridge the gap between the current limitations at CMJAH and the envisioned improvement in patient care through technological and procedural innovation. This transition underscores the need for a strategic approach to bolstering CMJAH's treatment planning capabilities while addressing staffing shortages and leveraging technological advancements.

Objectives include:

- To evaluate the technical feasibility of implementing a remote treatment planning service at CMJAH.
- To identify and address logistical and clinical challenges in integrating remote planning with existing systems.
- To assess the impact of remote treatment planning on treatment planning accuracy, efficiency, and patient throughput.

By setting these objectives, the research aims to navigate the difficulties of introducing a remote treatment planning service at CMJAH, tackling both the technical and operational hurdles. The intention is to construct a comprehensive understanding that not only validates the hypothesis but also contributes actionable insights into optimising cancer care delivery through innovative solutions.

Following this introduction, Chapter 2 embarks on a literature review, scrutinising the efficacy of existing remote planning practices and the utility of cutting-edge radiotherapy technologies. Chapter 3 elucidates the methodology for system commissioning and validation, emphasising the collection of precise commissioning data and the integration of Artificial Intelligence (AI) contouring software. Chapter 4 presents the results, evaluating the impact of this novel integration on treatment planning and patient care. Chapter 5 delves into a discussion of these outcomes in the broader context of CMJAH's operational challenges, offering insights into the potential advantages and constraints of the proposed solution. The conclusion in Chapter 6 encapsulates the study's

pivotal discoveries, reflecting on their clinical implications and proposing avenues for future research in the realm of radiotherapy treatment planning.

2 Theoretical Background

2.1 Literature Review

The advent of OTPS in the field of radiation oncology represents a transformative approach, enabling the provisioning of treatment planning expertise from distant locations, often spanning different regions or even countries. This model holds significant promise in providing equitable access to specialised care without necessitating the physical relocation of patients. The study by (Belard et al., 2011) provides insights into improving proton therapy accessibility through seamless electronic integration of remote treatment planning sites, highlighting the potential for remote treatment planning to enhance access to advanced treatment modalities. OTPS stands out due to its capability to grant institutions access to expertly crafted treatment plans, especially beneficial for locations facing limitations in local planning resources or specialised skills. However, the integration of OTPS is not devoid of challenges. It requires ensuring that proposed treatment plans align with the specific treatment units available at each institution. This necessitates robust communication channels between remote planners and local facilities to ensure the compatibility and practicality of the proposed plans. The study by (Granja et al., 2023) on access to general practitioners during the COVID-19 pandemic in Portugal underscores the importance of robust communication channels in remote healthcare delivery, emphasising the relevance of effective communication between remote planners and local facilities in OTPS implementation.

In the realm of data protection and privacy, the implementation of OTPS necessitates compliance with local government laws, such as the South African Protection of Personal Information Act (POPIA) (Republic of South Africa, 2013). The POPIA aims to regulate the processing of personal information and ensure the protection of individual privacy rights. As such, the sharing of patient data and information in remote treatment planning must adhere to the requirements outlined in the POPIA to safeguard patient confidentiality and

privacy. Thus, abiding by data-sharing policies remains a pivotal concern in the context of remote treatment planning services. The study by (Papoutsi et al., 2022) on implementing video group consultations in general practice during COVID-19 highlights the importance of data security and confidentiality in remote healthcare delivery, emphasising the relevance of adhering to data-sharing regulations in OTPS implementation.

Additionally, the delivery of personalised and tailored care remains a fundamental concern in the realm of OTPS. Effective collaboration between remote planners and local healthcare professionals becomes paramount in customising treatment plans to individual patient needs. This underscores the significance of seamless communication and coordination between remote planners and local care-giving teams to ensure patient-centric and optimised treatment plans. The study by Olsen et al. (Olsen et al., 2000), focusing on telemedicine in radiotherapy treatment planning, underscores the critical role of telecommunication systems and digital storage of relevant data in facilitating decentralized radiotherapy services. This research highlights the significance of an efficient and reliable telecommunication system between satellite units and the main radiotherapy clinic in ensuring the quality and effectiveness of remote treatment planning and delivery.

2.2 Beam data library: Commissioning and Data collection

The commissioning process for a medical linear accelerator involves the collection of comprehensive data to ensure accurate and safe radiation therapy treatment delivery. Commissioning is typically performed by medical physicists and is a critical step in establishing the clinical capabilities of the linear accelerator.

The commissioning process begins with the selection of appropriate equipment and tools for data collection. This may include ionisation chambers, electrometers, phantoms, and other measurement devices (Das et al., 2008). The choice

of equipment depends on the specific requirements of the linear accelerator and the desired accuracy of the commissioning data.

Data collection involves acquiring various beam parameters, such as PDD curves, beam profiles, OFs, and DLG (Das et al., 2008). These measurements are performed using the selected equipment and following established protocols and guidelines. The data collection process should be independent of the person collecting the data to ensure consistency and accuracy. The acquired data are then analysed and processed to generate commissioning data sets. This may involve data validation from so-called golden beam data sets, error correction, and data processing techniques to ensure the accuracy and reliability of the collected data (Das et al., 2008). The data sets are typically used to establish beam models and calibration curves for the TPS.

The commissioning process also includes the verification of the linear accelerator's mechanical and imaging systems (Netherton et al., 2019). These systems are tested to ensure proper functionality and alignment, which is crucial for accurate treatment delivery. It's crucial to understand that relying on vendor-supplied machine data is not an adequate replacement for the comprehensive commissioning of a Linac (Das et al., 2012). This principle emphasises the necessity of conducting detailed and site-specific commissioning processes to ensure the accuracy and safety of radiotherapy treatments. While vendors may provide beam distribution data, it is recommended to perform independent measurements to ensure the highest quality and accuracy of the commissioning data (Das et al., 2012).

The commissioning process is guided by established protocols and guidelines, such as those provided by the American Association of Physicists in Medicine (AAPM) and IAEA (Das et al., 2008). These guidelines provide recommendations on equipment selection, data collection procedures, and data analysis techniques.

2.2.1 Machine-Specific Characteristics

In light of the growing importance of networked solutions, it is essential to pay particular attention to the terminology assigned to the machines, encompassing the beam modalities, energies, and associated accessories like wedge filters, electron applicators, and MLCs. These labels should be meticulously detailed, free from ambiguity, and uphold consistency with the terminology employed within the Record and Verify (R&V) system.

Furthermore, the identification of the CT scanner employed for data acquisition is a requisite, particularly when the calibration curve, essential for converting Hounsfield Units (HU) into electron density (ED) or stopping power, necessitates an unequivocal association with the specific equipment used. This requirement is crucial to ensure accurate data interpretation. It might be necessary to assign multiple names, reflecting the utilization of diverse protocols, each calibrated with distinct curves, thereby eliminating any confusion.

To precisely simulate the permissible movements of local treatment machines, it is imperative to provide the TPS with highly accurate geometrical data:

- Establishing coordinate systems and defining translation and rotation scales (i.e. IEC 61217).
- Specifying the allowable movements and their respective ranges for various machine components, including collimator rotation, jaw asymmetry, gantry rotation, table rotation and translation.
- Giving particular attention to the MLC due to mechanical constraints like the minimum distance between opposing leaves and inter-digitation.
- Determining specific distances, such as those between the radiation source (or virtual source) and collimator, depending on the dose calculation algorithm. A detailed description of the machine head's components, including composition, shapes, and distances, is generally not necessary, except for certain Monte Carlo (MC) codes (Mayles et al., 2022).

2.2.2 Dosimetric measurements

The dosimetric data contained within the Eclipse Treatment Planning System (TPS) library rely significantly on the dose calculation algorithm. This dosimetric data primarily comprise the essential experimental dataset stipulated by the TPS vendor. Even for advanced models like Monte Carlo (MC) algorithms, this foundational experimental dataset includes items such as the reference calibration dose, D_{ref}, percent depth dose (PDD) data, off-axis profiles, and field output factors (OFs). This iterative fine-tuning continues until there's a precise alignment between the computed doses and the experimental findings (Das et al., 2008).

PDD is a measurement of the radiation dose absorbed at various depths in tissue/water relative to the dose absorbed at d_{max}. It helps in understanding how radiation dose attenuated as it penetrates tissue. Profiles refer to the distribution of radiation dose across a plane perpendicular to the beam axis. They are used to evaluate the uniformity and shape of the radiation beam. Off-axis factors indicate the dose variation relative to the central axis of the radiation beam at a specified depth. They are crucial for calculating doses received by tissues that are not located along the beam's central axis. OFs measure the dose delivered by the radiation beam relative to a reference condition, accounting for changes in field size (FS) or shape. They are essential for ensuring accurate dose delivery to the target area.

For precise modelling of the treatment machines, specific measurements are essential. These include considerations for the flattening filter's effect, the geometrical shape of the collimating device, and the transmission through blocks or trays. This correlation is critical and is established through calculations of treatment time or Monitor Units (MU), which in turn requires proper measurements of the dose output (Andreo et al., 2004). These measurements should ideally be performed using a computerised 3D water phantom (such as PTW BEAMSCAN), and the data can be electronically transferred to the TPS. However, maintaining self-consistency and ensuring that the entire dataset

represents the typical behaviour of the treatment machine is vital. This might involve some post-processing of the data (i.e. normalisation and smoothing), addressing minor asymmetries in the measurements.

This process of data measurement, entry, processing, and verification is time-intensive. It requires various software tools (which are mostly built into the TPS) to facilitate the interactive adjustment of coefficients to achieve a satisfactory alignment between computed and experimental dose distributions. A widely adopted method involves overlaying the computed and experimental PDD curves and profiles, ensuring that appropriate scales are used for an effective comparison.

The development of a beam model is dependent on the characteristics of the specific algorithm used and the degree to which it can be fine-tuned through various parameters. Given the nature of these parameters, the final beam model usually represents a balanced compromise. It is crucial to exercise due diligence and precision during this process, as it affects the accuracy of future dose calculations. Comprehensive documentation of the process is vital, as these records provide a crucial reference for any future software updates or modifications to the Linac's characteristics and accessories.

With the growing standardisation of equipment, it's feasible to utilise "golden data" (data deemed to be correct by the manufacturer) supplied by the manufacturer of the treatment machine. This can be especially advantageous when avoiding a full set of measurements if multiple machines within the same institution are "matched" (Das et al., 2012). However, it's advisable to conduct detailed verification based on a minimal set of measurements and to adjust data (or the machine) when unacceptable discrepancies are identified. In all cases, a best practice is to compare on-site measurements with data from equivalent treatment machines and resolve any notable discrepancies (Dufreneix et al., 2021).

2.2.3 Chamber volume correction

Utilizing specific ionisation chambers for dosimetry in small photon beams presents challenges due to volume averaging and the lack of electronic equilibrium. The perturbation of particle fluence by detectors within the medium calls for correction factors to mitigate this impact.

The correction factor for volume averaging accounts for the variance in the absorbed dose to water at a specified reference point within a water phantom, both in the absence and presence of a detector. This involves a comparison between the absorbed dose at this reference point and the average absorbed dose throughout the detector's sensitive volume, achieved by integrating the three-dimensional dose distribution inside the water phantom over the detector's volume (Palmans et al., 2018).

In the case of detectors such as plane-parallel ionisation chambers, diodes, or diamonds, which feature parallel electrodes aligned perpendicularly to the beam axis, this integration process is reduced to two dimensions, focusing on the detector's sensitive area that directly faces the beam. On the other hand, for cylindrical ionisation chambers, the integration covers the two-dimensional area of the sensitive volume that is projected orthogonally to the beam axis. This process incorporates a weighting function to accommodate various lateral displacements from the beam axis. High-resolution detectors are preferred for measuring lateral profiles, emphasizing the importance of the detector's orientation in these measurements (Ciancaglioni et al., 2012).

2.2.4 Multi leaf collimator (MLC) Transmission

MLCs are instrumental in sculpting radiation beams during radiotherapy to match the tumour's geometric profile while minimizing exposure to surrounding healthy tissues. An inherent characteristic of MLCs is the transmission of a fraction of the radiation beam through the leaves, termed MLC transmission. Despite the leaves being crafted from materials with high atomic numbers to effectively absorb radiation, they are not entirely efficient in attenuating the

entire radiation beam. These include scatter within the leaf material and the small gaps between the leaves, which allow a small percentage of the therapeutic beam to penetrate.

The MLC transmission equation is defined as:

$$T = \frac{D_{closed}}{D_{open}} \times 100 \tag{1}$$

where D_{closed} is the dose measured with the MLC leaves in the closed position and D_{open} represents the dose with the MLC removed or fully open (Boyer et al., 2001).

This phenomenon is crucial in treatment planning and dose calculation, contributing to the total dose a patient receives. Modern treatment planning systems (TPSs) compensate for MLC transmission by including transmission coefficients that estimate the dose contribution from the transmitted radiation. Precise modeling of MLC transmission is vital for the accuracy of dose calculations, especially in techniques like IMRT and VMAT, which employ MLCs dynamically to modulate beam intensity (Chen et al., 2015).

2.2.5 Dosimetric leaf gaps (DLGs)

DLGs represent the necessary additional space between the MLC leaves to accurately model the dose distribution around the edges of MLC-defined fields. They account for radiation transmission through the MLC leaves and the slight penumbra extension due to leaf end transmission and interleaf leakage, determined through commissioning tests like the sweeping gap technique. This technique quantifies the dose at the edge of the MLC field and compares it to the expected dose, informing the DLG value for enhanced dose calculation accuracy in the Treatment Planning System (TPS) (Chen et al., 2015).

The sweeping gap technique, crucial for determining the DLG in linear accelerators, assesses the DLG and the trailing effect between leaves of different multi-leaf collimator layers, such as in Halcyon^{TM} systems, highlighting an in-

crease in dose with trailing distance (Hernandez et al., 2021). The 'oscillating sweeping gap' approach, featuring a uniform MLC gap moving back and forth across the field during a gantry's full rotation, evaluates Linac performance and dosimetric parameters during VMAT delivery (Bhagwat et al., 2010).

Optimisation of the DLG setting for rounded leaf-end MLC systems using simple test fields has improved agreement between planned and delivered doses in QA evaluations (Yao and Farr, 2015). Additionally, the technique's utility extends to characterizing the Unity MLC and its computational models in Monaco and RayStation TPSs, where asynchronous sweeping gap tests yield results akin to dynamic experiments, confirming the effective tongue-and-groove width and MLC model's experimental data alignment (Kierkels et al., 2024).

2.3 Verification of TPS features

2.3.1 Confirmation of Non-Dosimetric Aspects

The non-dosimetric aspects of TPS commissioning were frequently overlooked, however, due to multiple publications of documents pertaining to the importance of these non-dosimetric elements are now considered integral to the commissioning process (Brunckhorst et al., 2008; Fraass et al., 1998; Andreo et al., 2004). This transformation is particularly evident in conformal radiotherapy (IMRT and VMAT), where geometric considerations hold great importance. It's important to note that the tests shown in Tables 1 to 3 serve as a guide to ensure proper operation of the TPS. The primary objective of conducting these tests are to explore the functionalities of the software and aid users in understanding the software's capabilities, constraints, and potential pitfalls.

2.3.2 Confirmation of Dosimetric Aspects

2.3.2.1 Calculation Checks

The assessment of the TPS is critically based on its capacity to accurately mimic the real dose distribution inside the patient, taking into account both

Table 1: Example of Assessments to Validate Input of Anatomical Patient Data into TPS (Mayles et al., 2022) .

Task	Scope	Method
Data Identification	Verify clarity and correctness of data identification within the TPS	Examine the structural labelling of images acquired from the imaging apparatus, encompassing patient, examination, series, and image identifiers. Utilize various protocols to import images into the TPS and validate their alignment with TPS data identifiers.
Image Series Validation	Assessing the consistency of data series	Generate scans with mixed attributes, including duplicated slices, distinct field views, different orientations, contrast variations, etc. Confirm that the TPS appropriately manages inconsistencies by either rejecting, warning, or processing these variations.
Patient Orientation Accuracy	Confirm accurate patient orientation handling by the TPS	Employ a test object with markers on various sides, scanning it in diverse patient orientations (e.g., supine/prone, head/feet first). Investigate how the TPS portrays these orientations in 2D and 3D reconstructions.
Geometric Data Representation	Validate absence of distance alterations or distortion	Compare measurements made on the imaging console with those computed in the TPS using suitable tools, potentially employing a phantom with known dimensions.
CT Density Consistency	Verify TPS density calculations against original HU data	Compare HU values from the CT console with those computed within the TPS. This comparison can preferably be done using a density phantom. Also, cross-reference HU values are manually derived from HU-to-density conversion curves to validate consistency.

Table 2: Example of Evaluations for Anatomical Data Processing (Mayles et al., 2022).

Evaluation Aspect	Scope	Procedure
Structure Delineation Precision	Assess the precision of manual or automated delineation options	Through patient or phantom images, perform 2D contouring using a variety of tools. Examine the alignment of the resulting contours with the original image.
Image Reconstruction Accuracy	Examine the accuracy of image reconstruction in different planes (e.g., sagittal or coronal)	Using patient or phantom images with identifiable landmarks in each plane, validate whether distances are faithfully replicated and the positions of each plane are satisfactorily represented. Additionally, analyse the positioning of reconstructed contours in relation to the reconstructed images.
Volume Expansion of Structures	Confirm the 3D process of adding margins to structures	Beginning with a basic structure, create supplementary structures by applying both symmetric and asymmetric margins across different slice thicknesses. Examine the results across various reconstruction planes to confirm, for example, that a point-like original structure with symmetric margins properly evolves into a spherical shape. Additionally, it's wise to evaluate the uniformity of outcomes when margins are added in a stepwise fashion compared to a single, comprehensive expansion. This approach ensures the structural integrity and accuracy of expansions in treatment planning simulations.
Image Registration	Validate the ability to merge images from different modalities into a unified patient model	Utilize patient or phantom images containing identifiable landmarks in both modalities. Compare the positioning of these landmarks in the two series post-registration, potentially leveraging different orientations (e.g., sagittal and coronal). Additionally, it may be beneficial to work with data sets showcasing known geometric relationships.

Table 3: Example of Evaluations for Representation of Beam Geometry (Mayles et al., 2022).

Aspect of Evaluation	Scope	Evaluation Method
Beam Positioning Evaluation	Evaluate various techniques for beam positioning and orientation definition	Utilize a patient or phantom model to place the beam employing diverse methods, including variations in beam orientation and position. Consider the faithful representation of beam movement longitudinally, even for various slice thicknesses, and simulate non-coplanar beams to examine graphical and numerical table rotation display.
Collimator Setting Assessment	Examine conventions for collimator aperture and rotation	For different techniques and SSDs, configure a rectangular field with known dimensions and appraise the graphical and numerical display. Ensure a comprehensive assessment, considering maximal and minimal FSs, and symmetric and asymmetric modes. Additionally, inspect how the display adjusts to collimator rotation in various planes.
MLC Examination	Examine the internal and external consistency of MLC files generated by the TPS	Based on given explicit or virtual field shapes, generate MLC leaf positions, considering different leaf fitting options and collimator rotations. Verify that the leaf positions are depicted as expected in graphical representations. Assess the minimum and maximum aperture limits and evaluate their relationship with primary jaws. Additionally, ensure consistency with the positions of the main jaws or backup jaws.

geometric and dosimetric uncertainties. The primary goal is to verify that the TPS does not contribute significant extra errors beyond those already present throughout the treatment cycle, from beam calibration to the conclusion of treatment. This ensures the reliability and precision of the TPS in delivering safe and effective radiation therapy. Typically, this entails achieving results falling within a range of approximately ±2 mm to ±3 mm concerning geometric accuracy, and within ±2% to ±3% regarding computed doses (McWilliam et al., 2015). The requisite level of precision relies on the specific clinical goals in question. For instance, a treatment plan for a stereotactic case would require significantly higher precision than one designed for palliative care (Mayles et al., 2022).

2.3.2.2 Algorithm Checks

The primary objective of algorithm testing is to validate the correct functionality of the algorithm. To achieve this, a comprehensive suite of tests and checks is meticulously designed and performed. Unit testing, as described by (Myers et al., 2012), involves verifying the correctness of isolated functions or methods within the algorithm. This form of testing is crucial for identifying and fixing errors at the smallest units of code, thereby ensuring the reliability of the basic operations the algorithm performs.

Integration testing, on the other hand, goes a step further by examining the interactions between these units or components (Perry, 2009). It focuses on detecting issues in the coordination between different parts of the algorithm, such as data flow errors or integration mismatches, which are not apparent during unit testing. This ensures that the algorithm operates cohesively as a whole.

Validation against benchmark datasets (Trabelsi et al., 2013) involves comparing the algorithm's outputs with known results from standard datasets. This test assesses the algorithm's effectiveness and accuracy in real-world scenarios, providing insight into how well the algorithm generalises beyond the test con-

ditions. It's an essential step for gauging the practical utility of the algorithm in accurately solving the problems it is designed for.

It's important to note that this testing framework doesn't guarantee that the computed results will always perfectly align with actual data, as many algorithms are inherently approximate and may not exhibit exact congruence with measurements (Andreo et al., 2004). Therefore, analyzing algorithm tests necessitates a thorough understanding of how the algorithm operates and what kind of results it should realistically produce. Users must recognize the inherent limitations and approximations of the algorithm to interpret its outputs correctly. This comprehensive approach to testing is indispensable for identifying any discrepancies between expected and actual outcomes, thereby facilitating the refinement and optimization of the algorithm (Langen et al., 2010).

2.3.2.3 Accuracy in advanced treatment techniques

The fundamental dose calculation algorithms employed in IMRT/VMAT plans closely resemble those used in non-IMRT plans. In both cases, they compute the cumulative dose resulting from modulated beams by aggregating numerous individual static beam dose distributions. Certain parameters take on heightened significance in IMRT/VMAT applications, primarily due to the frequent use of small apertures and a substantial number of MUs. For instance, in techniques like the sliding-window method and certain stereotactic approaches, meticulous adjustment of parameters such as leaf transmission and the so-called DLG becomes imperative (Hillman et al., 2018; Chauvet et al., 2005).

2.3.3 CT to ED data

Scanning an ED phantom using a CT scanner and importing the data into the TPS is a crucial step in accurately calculating radiation therapy treatment doses. This process involves acquiring CT images of the phantom, converting the CT numbers to relative electron density (RED), and importing the data

into the TPS for dose calculation.

To perform the CT scanning of an electron density (ED) phantom, specific scanning parameters such as slice thickness, pitch, and tube current should be carefully selected to ensure optimal image quality and accurate conversion of CT numbers to relative electron density (RED). It is important to note that the impact of scan parameters on the HU-electron density curve can vary. For example, most CT scanners use mAs modulation, meaning the mAs used on each patient and phantom might differ (Brevitt et al., 2021). Despite this variability, clinics often use a generalized calibration curve in the Treatment Planning System (TPS).

The calibration curve is typically established using a phantom with known RED values, which is scanned using the same CT scanner and scanning parameters as those used for the ED phantom. The HU values from the CT images of the calibration phantom are compared to the known RED values, and a calibration curve is generated. This curve is then applied to convert the HU values from the CT images of the ED phantom to RED values (Lim et al., 2022). Once the CT numbers are converted to RED, the data is imported into the TPS for dose calculation.

The TPS utilizes the RED values to accurately calculate the dose distribution within the patient's anatomy, taking into account tissue inhomogeneities represented by the RED values. This process allows for more precise treatment planning and dose delivery. The accuracy of the CT to RED conversion and the subsequent dose calculation depends on several factors, including the accuracy of the calibration curve, the quality of the CT images, and the proper selection of scanning parameters. Quality assurance measures should be implemented to ensure the accuracy and consistency of the CT scanning and data import process (Lim et al., 2022).

2.3.4 Auto contouring using AI.

Auto contouring in radiation oncology, particularly with the integration of AI technology such as RadAI from Siemens Healthineers (Siemens Healthineers, 2023), has emerged as a transformative approach in treatment planning and delivery. The utilisation of deep learning contouring algorithms has shown promise in improving automatic delineation for head and neck organs at risk, as highlighted in the study by (Dijk et al., 2020). This advancement addresses the limitations of existing clinical automatic contouring algorithms, such as atlas-based contouring, by leveraging deep learning techniques to enhance precision and accuracy in organ delineation.

Furthermore, the study by Rhee et al. (2020) demonstrates the development of an automatic contouring system for cervical cancer using convolutional neural networks, showcasing the potential of AI-based auto-contouring systems in accurately delineating clinical treatment volumes and normal structures essential for various radiation treatment planning techniques. Additionally, the clinical evaluation of deep learning and atlas-based auto-contouring of bladder and rectum for prostate radiation therapy, as discussed by (Zabel et al., 2021), emphasises the time-saving benefits of auto-contouring software for initial contour generation, while also highlighting the importance of quantifying workload changes during the editing phase.

The implementation of deep learning-based auto-segmentation for radiotherapy planning structures, as studied by (Wong et al., 2021), has demonstrated close similarity between deep-learning-based auto-segmented contours and expert radiation oncologist contours for the central nervous system, head and neck, and prostate organs at risk and clinical target volumes. This underscores the potential of AI-based auto-contouring in achieving consistency and accuracy comparable to expert manual contouring.

Moreover, the study by Shen et al. (2022) emphasises the reduction in radiation oncologists' contouring time as an inherent benefit of auto-contouring

of the organs at risk (OAR) for prostate cancer radiotherapy. This highlights the efficiency gains associated with AI-based auto-contouring, contributing to streamlined workflow and improved productivity in radiation oncology practices.

2.3.5 Workflow for a radiation oncology department.

The process within radiation oncology (general workflow depicted in Figure 1 begins with an initial consultation, where the radiation oncologist interacts with the patient to discuss the diagnosis and potential treatment modalities. This phase involves a thorough review of pertinent medical records and diagnostic exams to accurately assess the patient's condition Korreman et al. (2021).

Following the initial consultation, the patient proceeds to a simulation session where advanced imaging technologies, including CT scans, are utilised to delineate the treatment area. This imaging data is instrumental in creating a detailed 3D representation of the tumour and surrounding tissues (Douglass, 2022).

After the simulation, the radiation oncologist collaborates with a planner to contour the tumour and define organs at risk using specialised software tools found in the TPS. The objective is to devise an optimised treatment plan that delivers precise radiation doses to the tumour while minimising exposure to healthy tissues (Pasalic et al., 2018).

Once the treatment plan is formulated, it undergoes a review by the radiation oncologist and medical physicist to ensure its alignment with clinical objectives. Approval of the treatment plan signifies its readiness for implementation. Thereafter, the approved plan undergoes meticulous quality assurance checks to ascertain its accuracy and safety. This involves a comprehensive verification process of machine settings, meticulous scrutiny of dose calculations, and tailored patient-specific quality assurance to ensure the plan's reliability and precision (Chera et al., 2020).

The treatment phase ensues, where radiation therapy is administered according to the treatment plan. This stage involves the execution of radiation therapy by radiation therapists utilizing sophisticated equipment, such as Linacs or other specialised radiation delivery systems (Marks et al., 2013).

Post-treatment, the patient enters a phase of ongoing care, encompassing regular appointments to monitor treatment response. Continuous surveillance, including follow-up imaging studies and assessments, tracks the tumour's reaction to treatment and the patient's overall health, ensuring meticulous patient care throughout the therapeutic process within the realm of radiation oncology (Field et al., 2021).

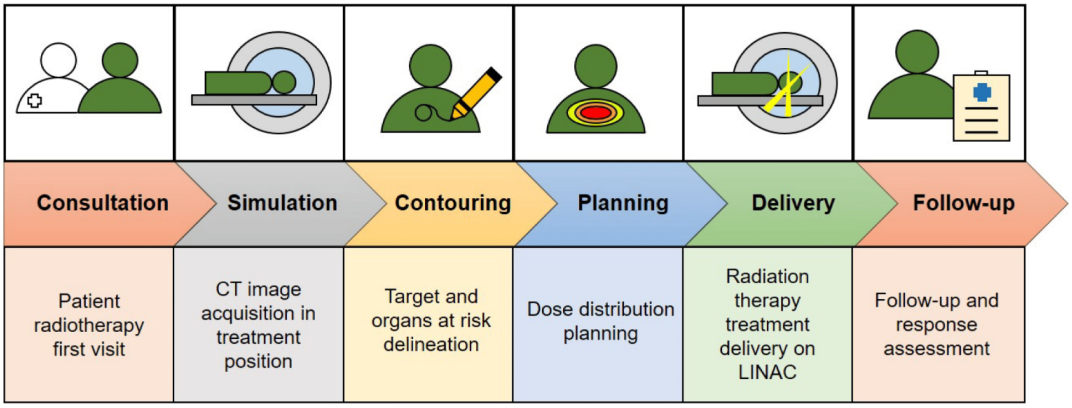


Figure 1: Typical workflow implemented in a radiation oncology department.

2.4 Linac Treatment Planning Modelling and Optimisation

In radiation oncology, ensuring the precision and reliability of treatment plans is paramount, necessitating thorough evaluation and verification of algorithms, dose calculation models, and optimisation techniques. The validation of the Acuros XB algorithm for dose calculation in heterogeneous media (Yu et al., 2019) exemplifies the industry's focus on accurate dose estimations. Verification of RapidArc treatment plans (Zhang et al., 2019) further highlights the significance of ensuring accuracy and safety in complex treatment delivery techniques.

Comprehensive validation is evident in the assessment of IMRT and VMAT delivery systems (Schoot et al., 2019), which underscores the necessity of end-to-end testing for treatment fidelity. Knowledge-based planning models (Smyth et al., 2013) are scrutinised for their potential to elevate plan quality and consistency, emphasizing the need for rigorous validation.

The Eclipse AAA algorithm's validation (Otto, 2007) and the verification of MC dose calculations (Raaymakers et al., 2017) also play crucial roles in ensuring precise treatment delivery. These methodologies reflect a commitment to accuracy, but they also underscore the evolving challenges and complexities faced in treatment planning.

One emerging challenge is the integration of adaptive radiotherapy (ART) techniques, which adjust plans based on changes in tumour size, shape, or patient anatomy throughout treatment. ART represents a significant advancement in personalised medicine but requires sophisticated algorithms to ensure treatment plans remain optimal and safe. These algorithms are necessary to dynamically adjust the treatment in response to anatomical changes, maintaining the precision and efficacy of the radiotherapy (Yan et al., 1997). Additionally, the increasing use of artificial intelligence (AI) in treatment optimisation presents both opportunities and challenges. AI can potentially enhance treat-

ment planning efficiency and outcomes but necessitates extensive validation to ensure reliability and clinical safety (Meyer et al., 2018).

Furthermore, patient-specific quality assurance (QA) processes are critical in verifying that the delivered dose conforms to the planned dose, especially for complex treatments. Techniques such as 3D dosimetry and in vivo dosimetry are gaining prominence for their ability to provide comprehensive QA (Létourneau et al., 2009).

As radiation oncology continues to advance, the integration of novel technologies and methodologies into treatment planning and delivery underscores the ongoing need for more validation and verification frameworks. These efforts are crucial for harnessing the full potential of these advancements, ensuring that innovations translate into improved patient care.

2.4.1 Analytical Anisotropic Algorithm (AAA)

Introduced in the early 2000s by Varian, the Anisotropic Analytical Algorithm (AAA) represents a significant advancement in the Eclipse Treatment Planning System (TPS) for radiation therapy. At its core, AAA utilises a sophisticated pencil-beam convolution and superposition method, designed to accurately model the dose distribution within a patient's body. This algorithm distinguishes itself by meticulously handling the dose's longitudinal (depth) and lateral (width and height) dispersal across different tissue densities.

Central to the AAA's operation is the concept of pencil beams, or "beamlets," which are small, discrete columns of radiation that collectively cover the treatment field. Each beamlet's influence on the dose distribution is calculated, considering the beamlet's cross-sectional area is approximately equivalent to a voxel within the patient model (Mayles et al., 2022). The mathematical expression that represents the dose contribution at any given point $\mathrm{P}(\mathrm{x}, \mathrm{y}, \mathrm{z})$ from a single beamlet located at $(\mathrm{x}', \mathrm{y}')$ can be formalised as:

$$D_\beta(x,y,z) = I_\beta(z) \iint \Phi_0(x',y') K_\beta(x-x', y-y', z) dx' dy' \tag{2}$$

In this equation:

- $\mathrm{I}_\beta(\mathrm{z})$ denotes the energy deposition function, characterizing the depth-dependent primary photon energy distribution,
- $\Phi_0(\mathrm{x}', \mathrm{y}')$ represents the initial photon fluence, assumed uniform across the beamlet's cross-section,
- $\mathrm{K}_\beta(\mathrm{x}-\mathrm{x}', \mathrm{y}-\mathrm{y}', \mathrm{z})$ is the scatter kernel, which quantifies the scattered photon contribution to the dose at point P from the beamlet $(\mathrm{x}', \mathrm{y}')$.

The AAA algorithm uses results from MC simulations to make its calculations, focusing on two main parts: I_β and K_β. These parts help the algorithm predict how radiation behaves. I_β is figured out from looking at how radiation decreases as it goes deeper into the body. On the other hand, K_β deals with how radiation spreads out and scatters. Initially, K_β used a mix of Gaussian functions to describe this scattering at different distances. It now uses six exponential functions that depend on the distance r from the centre of a beamlet to explain how scattering changes with space:

$$K_\beta(r,z) = \sum_{k=1}^{6} c_k \frac{1}{r} e^{-\mu_k r} \tag{3}$$

Where r is the radial distance from the beamlet centre, and μ_k and $\mathrm{c_k}$ define the attenuation and weight of each scatter component, respectively.

Adjustments for non-uniform media involve modifying the primary and scattered dose contributions according to local density variations, employing water-equivalent path length to scale lateral scatter. This adaptation ensures that the AAA can accurately account for heterogeneities within the patient's anatomy, providing a dose calculation that reflects the complexity of human tissues.

The algorithm also incorporates calculations for the main bremsstrahlung com-

ponent and secondary off-axis soft photon contributions, along with electron contamination, offering a comprehensive approach to dose modelling. Parameters critical to these calculations are rigorously derived from fundamental measurements, facilitated by sophisticated configuration software, underscoring the AAA's integral role in modern radiation therapy planning.

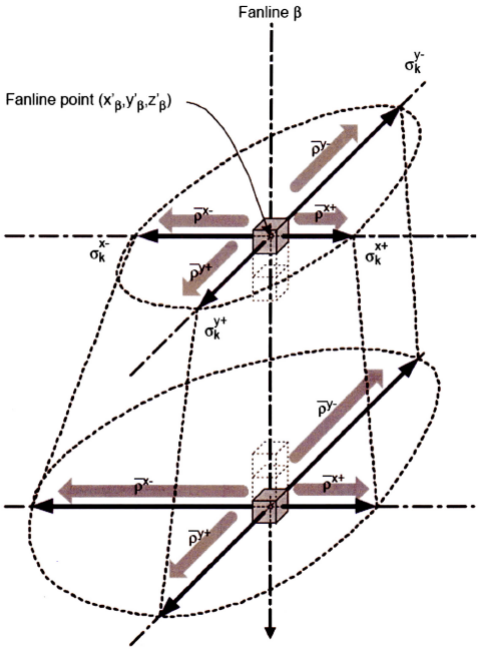


Figure 2: Illustration of the method used in the AAA algorithm (Mayles et al., 2022)

2.4.2 Beam Model Auto-Fitting Process

The AAA model is derived from extensive MC simulations, which analyse the complex interactions within the treatment unit's head. Varian's approach utilizes a sophisticated photon beam source model to represent the clinical beam. This model is comprised of several critical components: a primary photon source, a secondary photon source, an electron contamination source, and a wedge scatter source, which accounts for photons scattered by the hard wedge.

For each clinical beam under investigation, the model undergoes an auto-fitting process. This involves the dynamic adjustment of model parameters to accu-

rately reflect the specific phase space of the beam. This phase-space is essential for defining the beam's fluence and energy spectrum, tailored to each treatment unit and energy setting. The auto-fitting process is facilitated by a source model configuration program, which inputs specific measured beam data along with parameter values. These parameters, which can be manually defined by the researcher or automatically retrieved from a comprehensive parameter library, describe the physical characteristics of the beam and the geometry of its measurement (Varian Medical Systems, Palo Alto, CA, 2018).

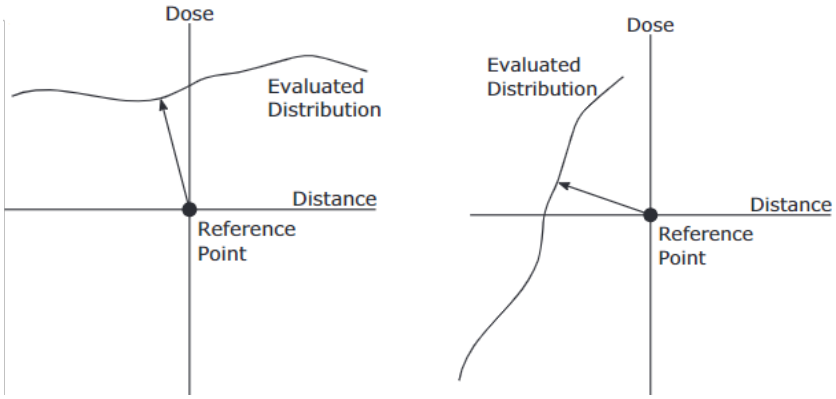
A key feature of the model is the segmentation of the clinical beam into finite-sized beamlets, as detailed in Section 2.4.1, referred to as β. The granularity of these beamlets correlates directly with the model's computational resolution, underscoring its flexibility in accommodating varying degrees of detail. Each segment of the beam—comprising both photon and electron components—is defined by unique beamlet intensities, offering a detailed account of the clinical beam's behaviour (Lee et al., 2001).

A crucial aspect of the auto-fitting process is the inclusion of an electron contamination source. This is vital for accurately modelling the dose distribution, particularly in the build-up region. Electron contamination arises from interactions within the Linac head and the air column before reaching the patient. The AAA handles this by modelling the total dose deposition as the superposition of doses from the primary and secondary photon sources, and the electron contamination source. This comprehensive approach ensures a more accurate representation of the clinical beam's behaviour, especially in areas where electron contamination significantly impacts dose calculations (Van Esch et al., 2006; Yang et al., 2004).

2.4.3 Gamma Index

Determining the accuracy of dose distributions in complex radiotherapy techniques like IMRT and VMAT presents a challenge. This is due to the dose gradients—areas where dose levels change rapidly or slowly—being unpredictable

across the treatment field (see Figure 3). To address this, the gamma index, γ, is employed as a tool to quantitatively compare the planned dose distribution against the delivered one. It helps to identify if a particular point, denoted as P_m, is accurately dosed, considering the surrounding dose gradient environment.



(a) Low-dose gradient. (b) High-dose gradient.

Figure 3: Illustrations of one-dimensional dose comparison analyses in scenarios with both shallow (a) and steep (b) dose gradients. The gamma value indicates how closely the evaluated distribution approximates the reference distribution. In mild dose gradients, the γ test primarily serves as a DD evaluation, whereas in pronounced dose gradients, it effectively measures the DTA.

The gamma index is calculated through a two-step process:

1. For every point P_c around P_m, where r is the distance between the measured and computed dose points, and d represents their dose difference, the gamma value Γ is calculated using Equation eq. (4), with Δd and Δr being the predefined dose and distance tolerances, respectively:

$$\Gamma(P_m, P_c) = \sqrt{\left(\frac{d}{\Delta d}\right)^2 + \left(\frac{r}{\Delta r}\right)^2}. \tag{4}$$

2. The gamma index γ for point P_m is then determined by finding the minimum Γ value among all surrounding points P_c, as shown in Equation eq. (5):

$$\gamma(P_m) = \min[\Gamma(P_m, P_c)]. \tag{5}$$

Gamma values ranging from 0 to 1 indicate a satisfactory match between the measured and planned doses, fulfilling the set criteria for both dose difference and spatial agreement. Values exceeding 1 signify a discrepancy, indicating the evaluated dose point falls outside the acceptable range of similarity. Essentially, γ illustrates the deviation between planned and delivered dose distributions, guiding the assessment as a circular (in 1D), spherical (in 2D), or hyper-spherical (in 3D) comparison metric (Miften et al., 2018).

The effectiveness of the γ test is influenced by factors such as the spatial resolution of the dose grid, the method of interpolation between dose points, and the dose grid spacing. Optimal spatial resolution, tailored to not exceed one-third of the DTA criterion, is crucial for dependable gamma analysis (Miften et al., 2018). Moreover, employing interpolation helps address alignment disparities between measured and calculated doses, balancing precision with computational efficiency. Adequate dose grid spacing, aligned with the DTA criterion, ensures comprehensive evaluation, avoiding overlooked discrepancies (Mayles et al., 2022).

3 Materials and Methods

In this chapter, we describe the materials and methods employed to commission and validate four Elekta VersaHD Linacs, focusing on the beam-matching process and subsequent TPS commissioning. Initial efforts concentrated on the precise acquisition of beam data for specific photon and electron energies, using advanced dosimetric equipment and techniques to ensure accurate and consistent treatment planning across all machines. The commissioning process included meticulous measurements of depth dose curves, profiles, and output factors, adhering to rigorous standards and guidelines to ensure treatment precision. Additionally, we employed MLC systems for precise field shaping and adopted a dual-phase approach for output factor measurement. This approach involves measuring output factors under different conditions to ensure comprehensive coverage of various field sizes and scenarios. The latter sections detail the validation of the Eclipse TPS through an end-to-end audit program, using phantoms that simulate patient anatomy to test the system's dose calculation accuracy. Through this systematic approach, the chapter aims to outline our material preparation, equipment commissioning, data collection methods, and the subsequent validation of the TPS, providing a clear framework for the reader on the methodologies underpinning this study.

3.1 Commissioning materials and equipment

The initial commissioning of four Elekta VersaHD Linacs involved a beam-matching process using a unified beam dataset to ensure consistency in treatment planning and delivery across all machines for specific energies (Xu et al., 2019). This strategic approach enhances treatment flexibility, allowing for seamless scheduling across different Linacs, thereby minimizing errors in the planning process without compromising treatment accuracy or patient safety.

Of the four Linacs, two have the following photon energies: three flattened (6x, 10x, and 15x) and two flattening-filter-free (FFF) options (6X FFF and 10X

FFF), all megavoltage (MV) energy beams. The remaining two Linacs feature a similar energy configuration, but with a variation in the flattened photon energies (6x, 10x, and 18x), alongside the same FFF energies (6X FFF and 10X FFF). Additionally, a range of six MeV electron energies (4, 6, 8, 9, 12, and 15 MeV) has been approved and commissioned for clinical applications. Given the project's scope, only focus was placed on two flattened (6x and 10x) photon beams and one flattening- filter-free (6X FFF) photon beam. Only a single Linac was used to obtain the required beam data as the above-mentioned energies were all matched in the remaining Linacs.

Each Linac has an Agility^{TM} head with a 160-leaf MLC system capable of speeds up to 3 cm/s across a $40 \times 40\,cm^2$ field-of-view (Thompson et al., 2014). It features a single pair of jaws moving in the opposite direction to the MLC leaves (Narayanasamy et al., 2017). The MLC is divided into two leaf banks, each with 80 leaves, producing a width of 5 mm at the isocentre. Additionally, the Linac includes a universal wedge compatible with 6x, 10x, 15x, and 18x open fields.

A PTW BEAMSCAN water tank was utilised to acquire beam data on the Linacs. The tank has a scanning volume of 500 mm (horizontal) x 500 mm (diagonal) x 415 mm (vertical) and is controlled by the BEAMSCAN software. The software communicates and controls the radiation detector's navigation and data collection through a motion control unit and has numerous features, including beam data post-processing. All beam scanning and data collection adhered to manufacturer manuals and professional guidelines, including AAPM Task Group Reports No. 40 (Kutcher et al., 1994) and No. 106 (Almond et al., 2008), as well as IAEA TRS-430 (Andreo et al., 2004) and TRS 483 (Palmans et al., 2018). These materials offer comprehensive recommendations for acceptance testing and beam commissioning measurements, covering both regular and small FSs.

The selection of dosimetric chambers for data collection, as detailed in Table 4, was guided by several critical considerations to ensure the highest standards

of accuracy and reliability in beam data acquisition. Firstly, the nominal sensitive volumes of the chambers were chosen to match the range of photon energies and FSs under investigation, optimising the detection efficiency for both flattened and FFF beams. The PTW Semiflex 3D TM 31021, with its smaller sensitive volume, was selected for its resolution in measuring steep dose gradients, making it ideal for profiles and OFs in smaller FSs ($> 3 \times 3\,\mathrm{cm}^2$) where precision is paramount (PTW Freiburg, 2024). Conversely, the PTW Farmer Chamber TM 30006, with a larger sensitive volume, was utilised for dose measurements in larger FSs.

Additionally, the use of a diamond detector, the PTW microDiamond TM 60022, for measurements in very small fields $\leqq 3 \times 3\,\mathrm{cm}^2$ addresses the challenges of volume averaging and perturbation effects (see Section 2.2.3) inherent to ionisation chambers. Its minimal sensitive volume and robust material properties allow for accurate dose measurements with negligible perturbation, ensuring fidelity in the characterisation of FFF beams and high-precision applications.

Configuring the source model for open fields in the Eclipse TPS required comprehensive beam data measurements, including depth dose curves, profiles, and output factors across various field sizes and depths. These measurements are crucial for accurately modeling the physical characteristics of the Linac beams, ensuring precise and reliable treatment planning (Varian Medical Systems, Palo Alto, CA, 2018).

3.2 Beam data collection: PDDs, profiles and Output Factors (OFs)

All PDD and profile measurements were performed at a fixed source-to-surface distance (SSD) of 100 cm. The FSs explored ranged from $1 \times 1, \mathrm{cm}^2$ to $40 \times 40, \mathrm{cm}^2$, ensuring a thorough evaluation across a broad range of treatment fields. Field size adjustments were executed with precision, using the collimator jaws for width modification along the IEC 61217-defined Y-axis (radial direction) and

Table 4: Detector Characteristics and Assigned Tasks for VersaHD Commissioning.

Type	**Model**	**Sensitive Volume**	**Diameter**	**Miscellaneous**	**Tasks Performed**
Cylindrical Ionization Chambers	PTW Semiflex 3D TM 31021	0.07 cm^3	4.8 mm	Aluminium	PDD, Profile and OF (Photon FS $\geq$ 3x3)
	PTW Farmer Chamber TM 30006	0.6 cm^3	2.3 mm	Aluminium	Dose measurements
	PTW Semiflex TM 31010	0.125 cm^3	5.5 mm	Aluminium	Independent dose measurement, Verification measurements
Diamond detector	PTW microDiamond TM 60022	0.004 cm^3	Active sensitive area: 3.8 mm^2	Synthetic single crystal diamond	PDD, Profile and OF (Photon FS $\leq$ 3x3)

the MLC leaves for length modification along the IEC-defined X-axis (transverse direction).

In adherence to the International Electrotechnical Commission (IEC) standard IEC 61217, the configuration of MLCs incorporated pairs of "guard leaves" strategically positioned near the field perimeters, under the direct control of the diaphragm jaws. These guard leaves provide an additional layer of precision, ensuring that the beam's edges are sharply defined and minimizing radiation spill outside the intended treatment area. Additionally, MLC leaves positioned outside the guard leaves, exactly 1.0 cm from the field edge determined by the jaw direction, are automatically retracted by the LINAC according to Elekta's operational protocols. This capability highlights the system's ability to dynamically adjust and maintain optimal field shaping across different FSs.

The diverse FSs required for the study were efficiently generated using Elekta's "Quick Beam" feature, accessible within the service mode of the LINAC. This feature offers a quick and efficient process for setting up and testing various field configurations. By utilizing the "Quick Beam" option, the study ensures that each FS is precisely adjusted and ready for the rigorous demands of radiation therapy, leveraging the LINAC's full range of capabilities.

The positioning of the cylindrical chamber (PTW Semiflex 3D 0.07 cc) was automatically corrected for the effective point of measurement using the PTW TruFix system integrated into the BEAMSCAN software. Both photon beam PDDs and profiles were mandatory and recommended as specified in the Varian Eclipse Photon and Electron Algorithms Reference Guide (Varian Medical Systems, Palo Alto, CA, 2018). Beam profiles were precisely measured in both cross-line and inline directions for specified FSs and scanning depths (d_{max}, 5, 10, 20, and 30 cm). For the largest FS ($40 \times 40, cm^2$), diagonal profiles were obtained at the same depths using open beams.

Before initiating measurements, a central axis correction for the water phantom was conducted for each beam energy through the PTW BEAMSCAN software to guarantee measurement accuracy. This correction process was critical in

aligning the detector accurately within the centre of the radiation field, a prerequisite for obtaining precise and reliable data. The procedure employed two distinct measurements to achieve this alignment.

The first step involved measuring a FS of $10 \times 10, \mathrm{cm}^2$, where the software analysed the in-plane and cross-plane profiles. This analysis enables the software to identify any lateral shifts between these profiles, facilitating adjustments to ensure the detector's placement at the radiation field's geometric centre. Following this initial adjustment, the process continued with two cross-plane measurements aimed at identifying any rotational deviations in the detector's positioning. These measurements were crucial for detecting and correcting minor rotational shifts, which, if left unaddressed, would have compromised the accuracy of the beam data collected.

For FSs $\leq 3 \times 3\,\mathrm{cm}^2$, a PTW microDiamond 0.004 cc detector was chosen due to having a small nominal sensitive volume of 0.004 cc and being the smallest available detector. The results obtained from the aforementioned detector underwent correction for volume averaging and perturbation effects (refer to Section 2.2.3) in line with the methodology outlined in IAEA TRS 483 (Palmans et al., 2018).

For FSs $\geq 3 \times 3, \mathrm{cm}^2$, beam data was gathered using a step-by-step scan mode (to ensure enough charge is collected at each position) and a dual ionisation chamber setup, incorporating PTW SemifFlex 0.07 cc 3D ionisation chambers for both field and reference measurements. Scan speeds were adapted based on dose rate and FS variations to maintain beam data quality. For profiles larger than the water tank dimensions, such as $40 \times 40, \mathrm{cm}^2$ inline, cross-line, and diagonal, the tank was shifted off-axis, half of the profile was measured and then mirrored to obtain the full profile. Mirroring assumes beam symmetry and may miss asymmetries and edge effects, potentially affecting profile accuracy and beam model precision.

OFs were determined at a standardised SSD of 90 cm and a depth of 5 cm. Per Varian's recommendation (Varian Medical Systems, Palo Alto, CA, 2018),

small field measurements (FSs $\leq 3 \times 3\,\mathrm{cm}^2$) were obtained utilizing the PTW microDiamond 0.004 cc detector. Square FSs were selected as a reference for comparison purposes. The results underwent adjustments to account for volume averaging and perturbation effects, adhering to the methodology prescribed by the IAEA TRS 483 (Palmans et al., 2018). For FSs ranging from $5 \times 5\,\mathrm{cm}^2$ up to the maximum open FS of $40 \times 40\,\mathrm{cm}^2$, the measurements were carried out utilizing the PTW Semiflex 3D 0.07 cc ionisation chamber. All OF measurement data was normalised to the reading derived from the $10 \times 10\,\mathrm{cm}^2$ FS.

3.3 MLC transmission and DLGs

MLC transmission measurements, detailed in Section 2.2.4, were performed separately for each of the MLC leaf banks. Initially, leaves were moved to the extreme right of the leaf bank for one measurement and then to the extreme left for another, ensuring that one leaf bank exclusively obstructed the field in each case. The MLC transmission value was determined by averaging the results from both sets of measurements. Throughout this process, a PTW Farmer 0.6 cc ionisation chamber was employed at a depth of 10 cm within the PTW BEAMSCAN water tank to facilitate measurements for all photon energies. Notably, the anticipated MLC transmission values were held within a threshold of 2% (Galvin et al., 1995)

The reference to AAPM TG 50 provides a historical benchmark for MLC transmission, but it predates the introduction of the Agility MLC system on the Elekta VersaHD Linacs. Studies have shown that the Agility MLC exhibits improved transmission characteristics compared to older MLC systems. Specifically, the Agility MLC has a measured transmission of less than 0.5%, significantly lower than the values reported in TG 50. This improvement is due to the advanced design and materials used in the Agility MLC, which enhance its performance and reduce transmission and leakage (Kong et al., 2015; Park et al., 2014; Cutright et al., 2013).

Employing the same experimental setup, the DLG factor (refer to Section 2.2.5), accounting for the transmission through the leaf ends, was initially assessed for all required photon energies. This assessment employed the sweeping-gap technique, utilizing Varian's Digital Imaging and Communications in Medicine (DICOM) plan files which were imported into Monaco, the TPS used clinically at CMJAH, and subsequently exported to Mosaiq. The choice of Monaco and Mosaiq was dictated by their current use within the hospital's clinical workflow. The use of Monaco and Mosaiq streamlined the process of running the plan and collecting the required data.

The sweeping-gap method entailed successive movement of MLC gaps of varying sizes (5, 10, 16, 20, and 30 mm) from left to right across a rectangular field, delivering a cumulative dose of 200 MU per plan. At each MLC gap size, the corresponding output reading was measured through the employment of the PTW Farmer 0.6 cc ionisation chamber as well as a PTW Unidose T10008 electrometer.

3.4 Validation of the Eclipse TPS

The validation of the Eclipse TPS was a critical step in the commissioning process, ensuring accurate modelling and prediction of radiation dose distributions for clinical treatments. This study utilized both solid water slabs and the Shane phantom for a comprehensive validation approach. The solid water slabs provided a controlled environment to assess the TPS's dose calculation accuracy in homogeneous media, which was fundamental for evaluating basic beam parameters like depth dose curves and dose profiles under simplified conditions. These measurements established a baseline for the TPS's performance, confirming its capability to accurately calculate doses in straightforward, homogeneous scenarios.

In contrast, the Shane phantom was employed for its ability to simulate the anatomical complexities of the head and neck region with high fidelity, thus serving a more clinically relevant validation role. It allowed for the assess-

ment of the TPS's handling of heterogeneous tissue densities and complex geometries, closely mirroring real patient treatment scenarios. This approach not only tested the system's accuracy in mapping CT numbers to ED values but also evaluated dose distribution calculations around various tissue types. Through these dual validation methods, we aimed to verify the TPS's accuracy and reliability over a range of conditions—from basic to complex—ensuring a thorough assessment of its clinical utility.

With the foundational understanding established through basic validation using solid water slabs, we advanced to detailed validation employing the Shane phantom. This dual-phase approach,using homogeneous and inhomogeneous phantoms, ensured the TPS was evaluated for accuracy and reliability, demonstrating its readiness to support precise and effective patient treatments.

Subsequent to the beam data collection and treatment beam modelling, the next step in the TPS commissioning was to undertake validation measurements and tests. For this purpose, the "National End-to-End Audit Programme for Dose Delivery Using IMRT through On-Site Visits to Radiation Therapy Institutions," developed by the IAEA, was adopted (Clark et al., 2019).

The Shane phantom, which emulates the head and neck anatomy of an average radiotherapy patient with remarkable detail, incorporated precisely calibrated reference plugs for cortical bone, trabecular bone, lung inhalation, and lung exhalation simulations. Additionally, it included a water-filled vial crucial for constructing a conversion curve to map CT numbers to RED, further underscoring the system's applicability to clinical practice.

In preparation for detailed validation of the TPS, a series of rigorous validation measurements were meticulously planned and executed. The primary objective of these measurements was to evaluate the TPS's precision and reliability in simulating and calculating radiation dose distributions across a range of clinically relevant scenarios. This validation process began by adopting the IAEA End-to-End methodology (Clark et al., 2019), which provided a comprehensive and standardized framework for system evaluation. To assess the



Figure 4: CIRS Shane phantom depicting all elements.

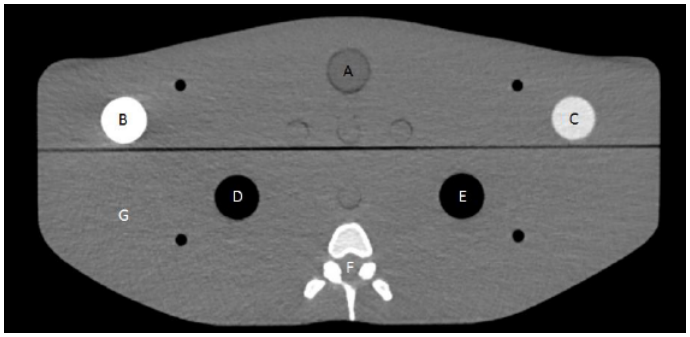


Figure 5: CT scan of the SHANE phantom's shoulder region showing electron density plugs: (A) water, (B) cortical bone, (C) trabecular bone, (D) lung exhale, (E) lung inhale, (F) spinal cord, (G) soft tissue (Clark et al., 2019).

TPS's ability to accurately map CT numbers to ED values, the Shane phantom was employed, specifically chosen for its ability to replicate the anatomical complexities of the head and neck region with high fidelity. Additionally, the development of a four-field box plan using a slab water phantom, encompassing a variety of FSs and orientations, facilitated a thorough examination of the TPS's operational performance under diverse treatment conditions. These preliminary steps were instrumental in facilitating a comprehensive analysis of the TPS, underscoring the necessity for precise adjustment of dose leakage and DLG values and the validation of the AAA calculation model with the data obtained during commissioning.

3.4.1 CT-ED calibration curve

As described in section (Section 2.3.3), mapping the HU to RED should be carried out for accurate dose calculation for all heterogeneities found in datasets encountered in the clinic for patient treatment. To this end, the CT to RED curve was obtained using CIRS M062 phantom (Figure 6) on two CT scanners, a Toshiba Aquillion at 120 kVp X-ray tube settings and a Siemens SOMATOM at 120 keV X-ray tube settings.

To further verify the validity of the curve obtained, the CT to ED curve obtained from the CIRS M062 from the Canon Aquillion LB CT scanner, was compared to the CT to ED curve obtained from the SHANE CIRS phantom from the Canon Aquillion LB CT scanner.

3.4.2 Verification of the AAA calculation model based on commissioning data.

Integrating the beam model developed by Varian into Eclipse, and subsequently standardizing the model for the four matched Linacs, was a pivotal moment in the commissioning process. This standardised model allowed for accurate dose calculations and streamlined the verification of data transfer across different orientations, ensuring compliance with the IEC 61217 conven-

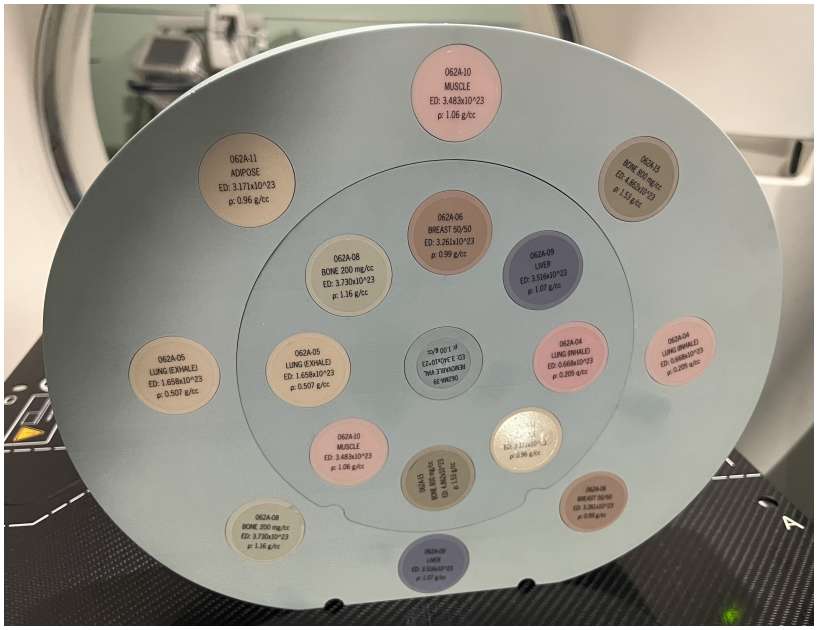


Figure 6: CIRS M062 phantom for CT to RED/Mass density conversion curve measurements scanned on a Canon Aquillion LB CT scanner.

tion scales on all platforms (Eclipse TPS, Mosaiq R&V, and Elekta Linac).

A series of commissioning plans were devised to assess the beam model's accuracy and the system's ability to replicate clinical treatment conditions, targeting diverse couches, collimator, and gantry orientations. This approach was designed to verify the consistency of the convention scales and the integration of the Eclipse TPS, Mosaiq R&V, and Elekta Linac in simulating real-world clinical scenarios.

The four-field box plan was created on a slab water phantom (Figure 7). Field 1, was $10 \times 10\,\mathrm{cm}^2$ size with couch rotation of 270° and gantry 20°. Field 2, was $5 \times 20\,\mathrm{cm}^2$ size with collimator rotation of 330° and gantry 90° Field 3, was 20x20 cm2 size with gantry 180° passing through the couch. Field 4, was $3 \times 3\,\mathrm{cm}^2$ field with gantry 270°.

These configurations were specifically selected to encompass a broad spectrum of clinical scenarios, from standard treatments to complex orientations, ensuring the beam model's robustness and the system's versatility in adapting to varied clinical demands.

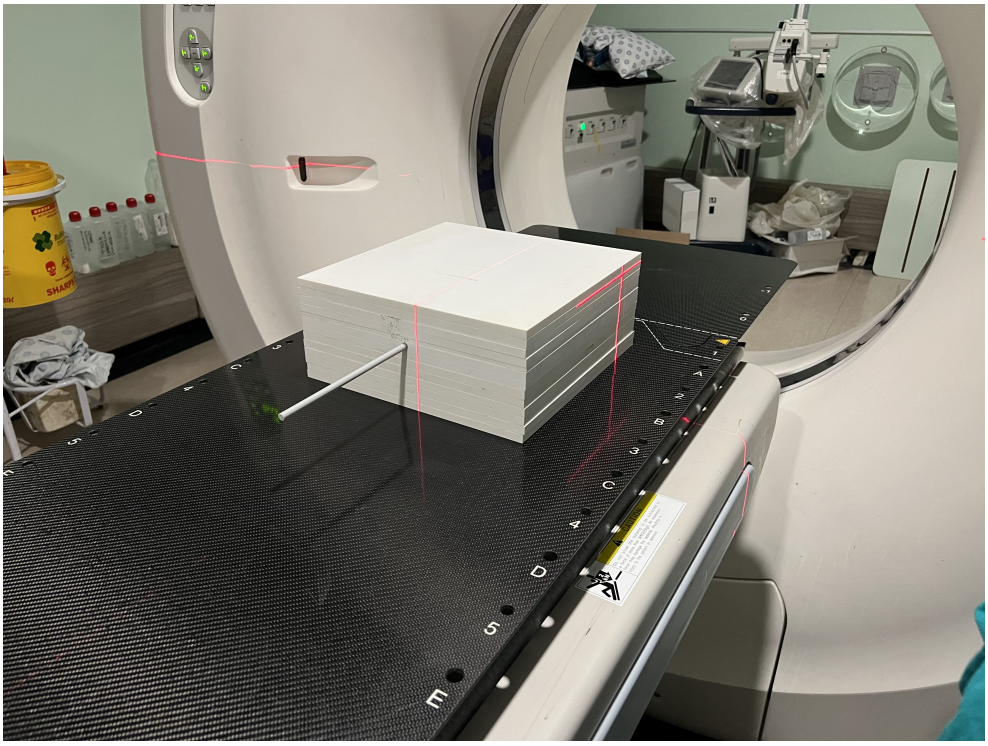


Figure 7: RW3 slab phantom with an insert suitable for a PTW Semiflex 0.125 cc chamber at 5 cm depth scanned on a Canon Aquillion LB CT scanner.

3.4.3 MLC parameter fine-tuning

Two clinical VMAT plans, one prostate (1 arc) and one head and neck (2 arcs) were generated for each energy, and their respective beams were transferred onto the RW3 slab phantom. An iterative course of action was undertaken to validate the dose of the plans and fine-tune the DLG for each energy. The meticulous calibration of DLGs pertained solely to the IMRT/VMAT plans, given their marginal influence on the dosimetry of fundamental 2D/3D plans (Zhang et al., 2019).

Replicating the scanning setup of the RW3 slabs on the treatment couch, the point dose measurements were obtained for each energy and the results were compared to the TPS system's calculated values. The plan beams were transferred onto the PTW Octavius 4D phantom, and treated and the measured dose distribution was assessed through the PTW Verisoft software, per the delineated protocols from Task Group Report No. 218 (Miften et al., 2018).

Subsequently, guided by the point dose measurements and the Verisoft results, the DLG for MLCs were adjusted within the Eclipse TPS.

The treatment plans were re-optimised and recalculated using the revised MLC DLG value. This process was repeated iteratively until the new DLG value resulted in a measured dose distribution that met or exceeded a 95% gamma passing rate across all commissioning plans for each specific energy. The gamma assessment in Verisoft software followed a criterion that included a 3% global dose difference, a 2 mm distance-to-agreement (DTA), and a 5% dose threshold, as outlined in (Miften et al., 2018).

3.4.4 IAEA End-to-End methodology

The clinical test case is specifically devised to replicate an IMRT H&N plan for a patient exhibiting a nasopharyngeal tumour. Data set of the CIRS Shane phantom was obtained from the Toshiba Aquillion CT scanner at CMJAH. A member of the Varian team provided a structure set of the phantom that contained 17 structures associated with targets and OARs. The structure set contained a set of contours, including CTVs, planning target volumes, and structures about the ion chamber's measurement positions. These volumes and their respective ID's had remained unaltered to conform as closely as possible to the method (Kazantsev et al., 2020).

The CT data structure sets used in this study were provided by Catharine Clark, one of the authors of the report titled "National 'End-to-End' Audit Programme for Dose Delivery Using Intensity-Modulated Radiation Therapy through On-Site Visits to Radiation Therapy Institutions" (Clark et al., 2019). The CT dataset (obtained from scanning the CIRS SHANE phantom on the Canon Aquillion LB CT scanner) were imported into Eclipse as a new patient, which provided a means to test if the CT export and TPS import protocols functioned as expected. The volumes of individual structures were cross-checked against predetermined values characteristic of the CIRS SHANE phantom (Table 5) and ensured completeness without significant alterations.

Although the method allows for additional planning structures to be introduced, no other structures were added as the scope of the project did not require any alterations.

Machine calibration verification was done using IAEA TRS-398 (IAEA, 2001) protocol. This was done for each of the relevant energies ensuring that the machine was calibrated to deliver 1 Gy at D_{max} for 100 MU, a FS of $10 \times 10\,cm^2$ at an SSD of 100 cm. Initially received from Varian consultants, the preplan underwent recalculation employing the planning CT data and standard grid resolution for H&N IMRT plans. A member of Varians team scrutinised this recalculated plan, evaluating its adherence to planning constraints. If needed, potential re-optimisation steps were considered. Once finalised, the auditor recorded DVH values for all targets (D98%, D50%, and D2%) and OAR in the IMRT audit reporting form. Patient-specific IMRT/VMAT plan QA procedures were executed, and outcomes were documented.

The measurements with the SHANE system utilised a 0.125 cc ionisation chamber which have been proven to be effective for pretreatment dose verification for advanced techniques (Kakade et al., 2019). Using the corresponding chamber cavity rod, the chamber was positioned into one of four designated SHANE measurement channels. These positions were mentioned in Table 5 and were identified by the prefix IC.

For accurate placement, the chamber needed to be inserted fully into the cavity rod (Figure 8b). The IAEA recommended fixing the chamber cable by taping it to the treatment couch to secure the chamber and prevent movement during measurements. The remaining SHANE channels were to be plugged into the same density material as the main body of the phantom. This procedure was repeated for the SHANE irradiations in the three remaining channels.

Table 5: CIRS Shane phantom structure with corresponding volumes and TPS limits.

Structure name	**Description**	**Volume cm³**	**Min cm³**	**Max cm³**
PTV_7000	Nasopharynx primary plan target	88.5	87.6	89.4
PTVn1_6000	Involved nodes plan target volume	411.6	397.2	426
PTVn2_5400	Elective nodes plan target volume	260.3	244.7	275.9
SpinalCord	Spinal cord organ at risk	4.9	22.8	27
SpinalCord_03	Spinal cord Plan Risk Volume 3mm	55.1	50.1	60.1
BrainStem	Brain stem organ at risk	43.9	42.6	45.2
BrainStem_03	Brian stem Plan Risk Volume 3mm	72.5	71.4	73.6
Parotid_L	Contralateral left parotid	19.7	18.9	20.5
Parotid_R	Ipsi lateral right parotid	23.4	22.5	24.3
IC_PTV_7000	Ion chamber volume in nasopharynx	0.13	0.1	0.2
IC_PTVn1_6000	Ion chamber volume in involved nodes	0.13	0.1	0.2
IC_PTVn2_5400	Ion chamber volume in elective nodes	0.13	0.1	0.2
IC_SpinalCord	Ion chamber volume in spinal cord	0.13	0.1	0.2
Channel_1	Channel for IC_PTV_7000	42	37.8	46.2
Channel_2	Channel for IC_PTVn1_6000	42	37.8	46.2
Channel_3	Channel for IC_PTVn2_5400	42	37.8	46.2
Channel_4	Channel for IC_SpinalCord	42	37.8	46.2

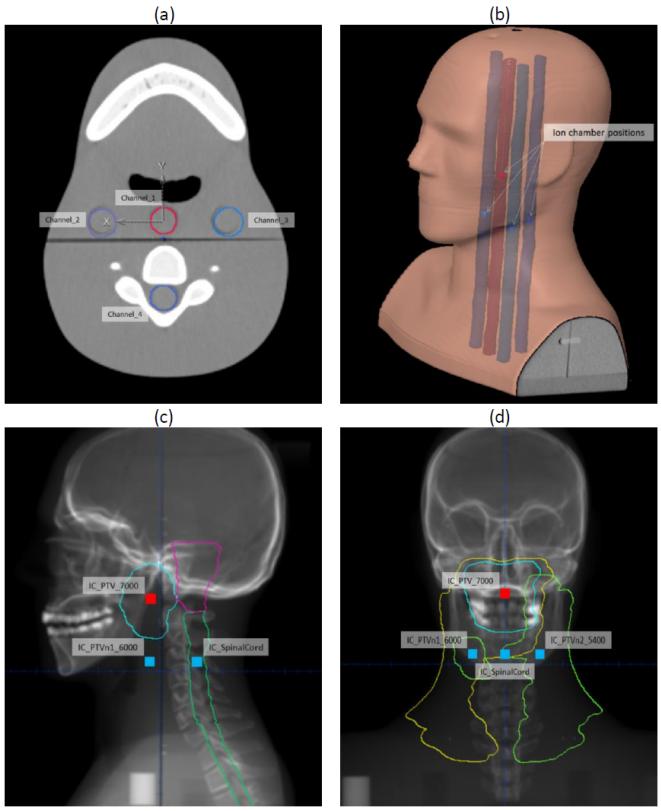


Figure 8: CT examination of the CIRS Shane H&N phantom displaying the ion chamber channels' locations and their respective positions, depicted in (a) the transverse plane, (b) 3-D display, (c) sagittal view, and (d) coronal view (Kazantsev et al., 2020).

4 Results and Discussion

In the commissioning process of the Eclipse system, a vast array of measurements (profiles, PDDs and OFs) were obtained to ensure the accuracy and reliability of the beam modelling data. A few graphs and data have been selected to illustrate examples or highlight notable errors/deviations from expected outcomes. Also presented in this work are the commissioning results covering all aspects of Eclipse commissioning, from beam data acquisition to model validation. The final section presents work/results focusing on the feasibility aspects of implementing the remote service in the department.

4.1 Commissioned beam data

Before their integration into the Eclipse system, all necessary data entries for beam modelling were thoroughly validated. As an example, Figure 9 displays the measured Percent Depth Dose (PDD) curves for 10X photons at various FSs. Additionally, the 10X photon beam profiles for a $3 \times 3\,\mathrm{cm}^2$ FS, measured at depths of $\mathrm{d_{max}}$, 5 cm, 10 cm, 20 cm, and 30 cm, are presented in Figure 10. Comprehensive beam profiles, PDDs, and Output Factors (OFs) for each energy level were acquired for FSs ranging from $1 \times 1\,\mathrm{cm}^2$ to $40 \times 40\,\mathrm{cm}^2$.

Before OF measurements were taken, scans were conducted for small fields of $1 \times 1, \mathrm{cm}^2$ to verify the central position of the PTW microDiamond 0.004 cc detector and confirm the field size (FS), as shown in Figure 11. The analysis of the profile displayed that the profile had a size of 1.024 cm x 1.092 cm for in-plane and cross-plane respectively. This minor increase in the FS, resulting in a deviation of no more than 1 mm from the expected nominal size, is consistent with expected results for small field sizes. Such deviations are typically attributed to factors including the lack of lateral electronic equilibrium, volume averaging effects of the detector, and the geometric setup affecting the beam penumbra (Palmans et al., 2018).

Figure 12a provides an overview of the OF for open fields for all three energies

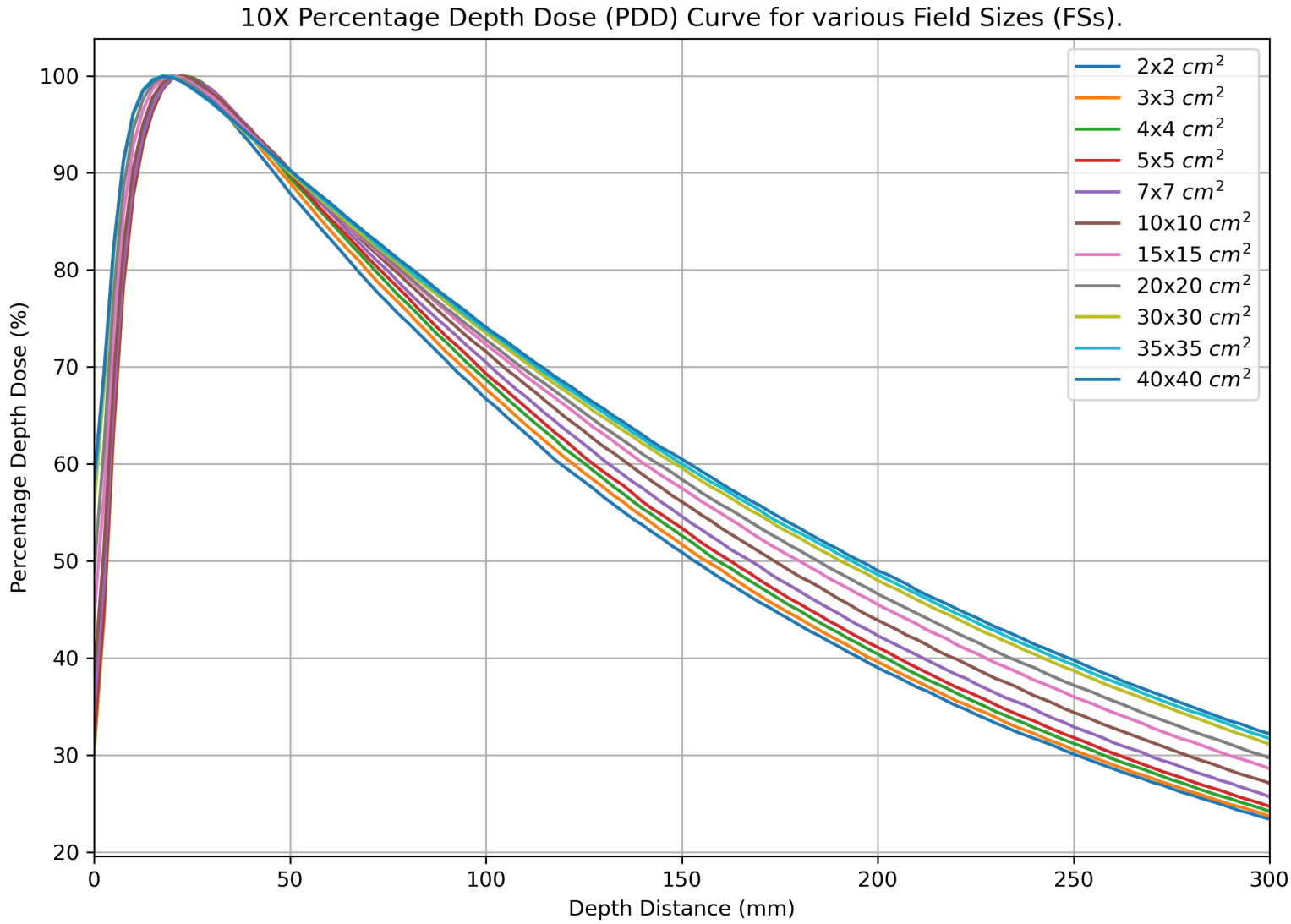


Figure 9: 10X PDD for various FS using the PTW microDiamond 0.004 cc for FSs between $2 \times$ cm^2 - 4×4 cm^2 and the PTW Semiflex 3D 0.07 cc (both chambers shown in Table 4) for FS between 5×5 cm^2 - 40×40 cm^2 and at an SSD of 90 cm.

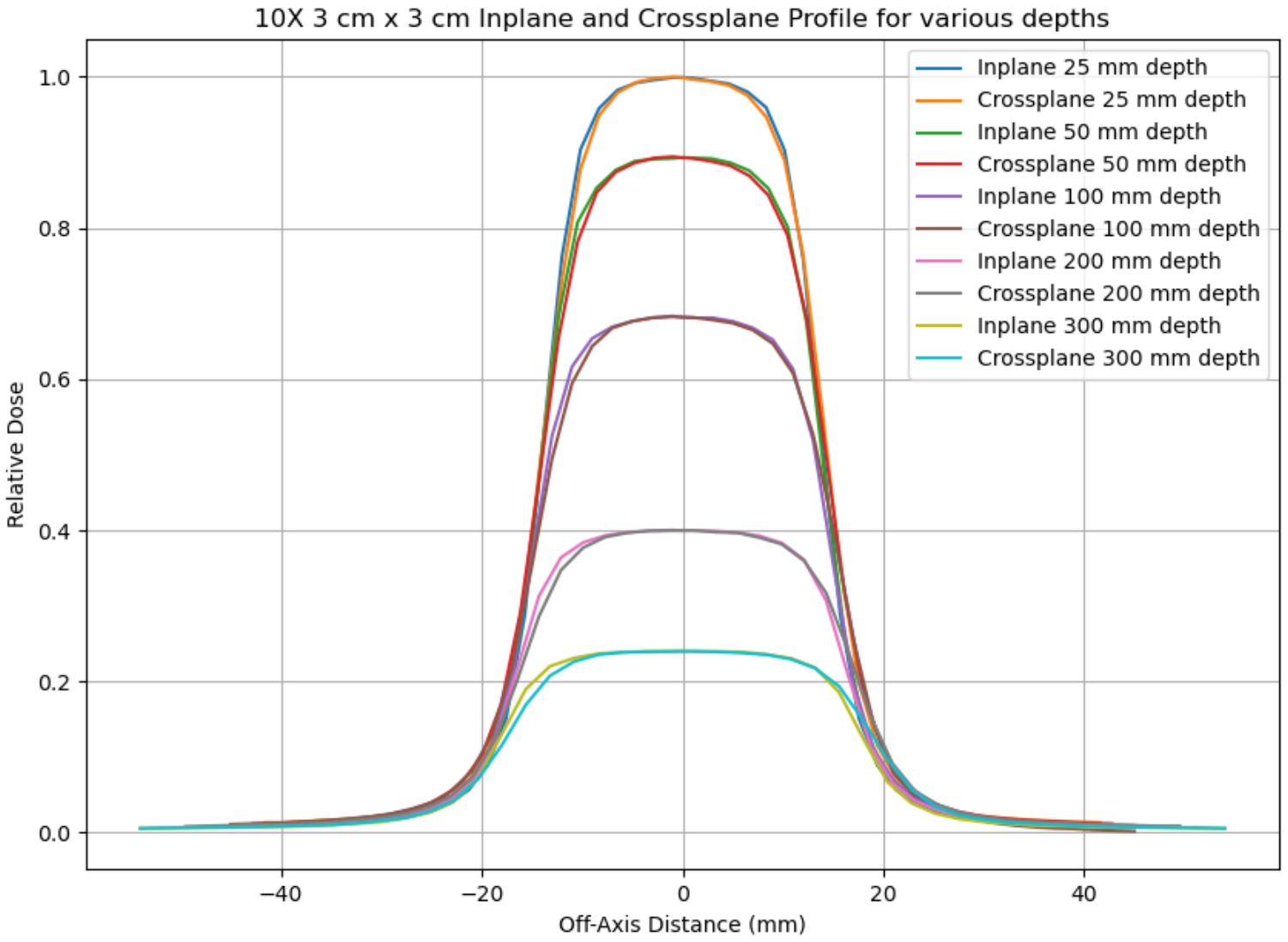


Figure 10: 10X inline and cross-line profiles for $3 \times 3\,\mathrm{cm}^2$ FS at depths $\mathrm{d_{max}}$, 5 cm, 10 cm, 20 cm and 30 cm using the PTW microDiamond 0.004 cc (shown in Table 4) at an SSD of 90 cm.

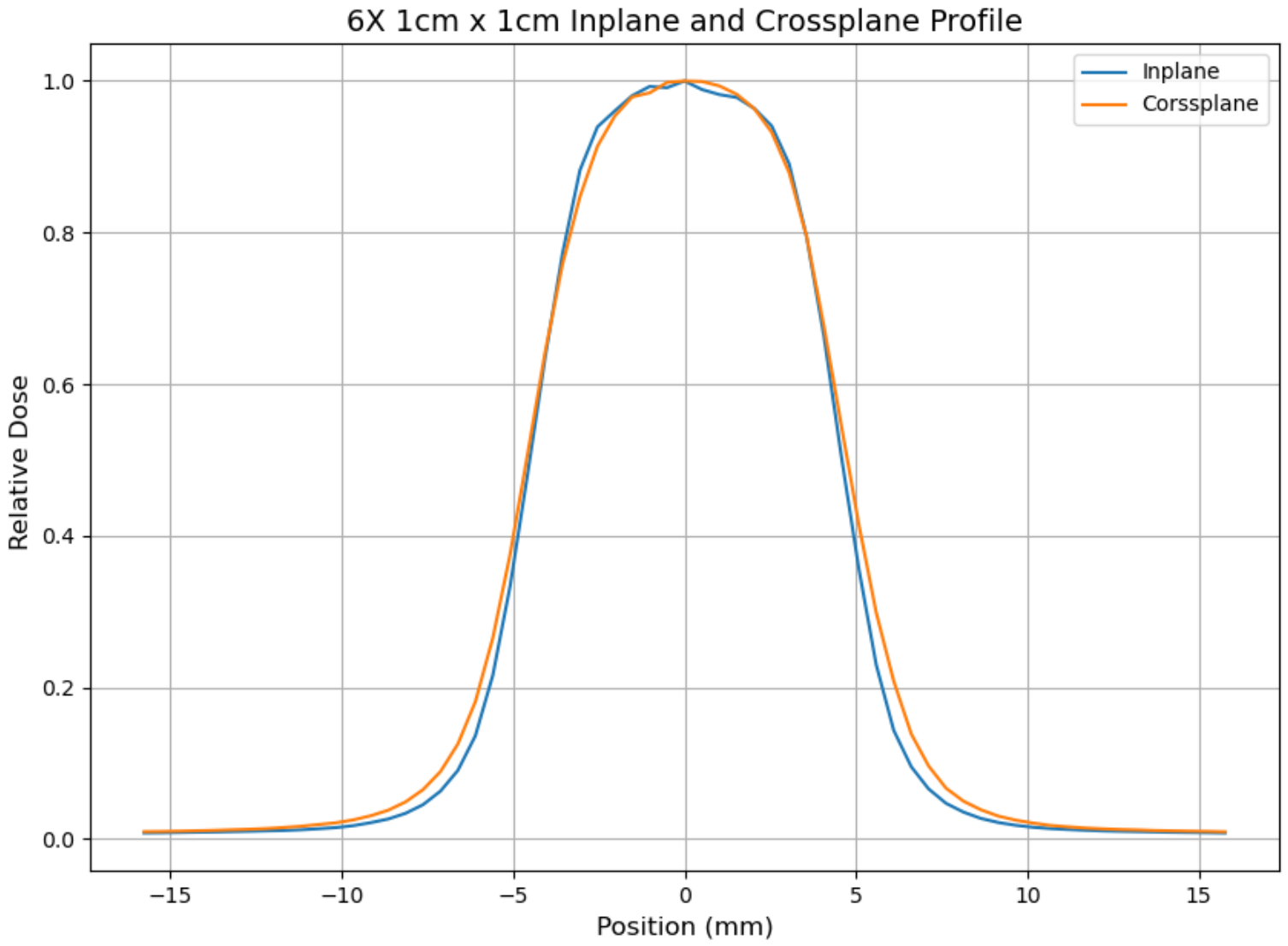


Figure 11: 6X cross-plane and in-plane profiles of $1 \times 1\,\mathrm{cm}^2$ FS scanned with PTW microDiamond 0.004 cc (shown in Table 4) at an SSD of 90 cm, depth 10 cm.

taken at an SSD of 90 cm, and depth of 10 cm, and Figure 12b depicts the difference between the Accelerated Go Live (AGL) OFs from Elekta. As seen from Figure 12a 10X and 6X FFF measured OFs displayed the most deviation from the AGL data at 3.3 % and 3.5% respectively, at FS of $1 \times 1\,\mathrm{cm}^2$.

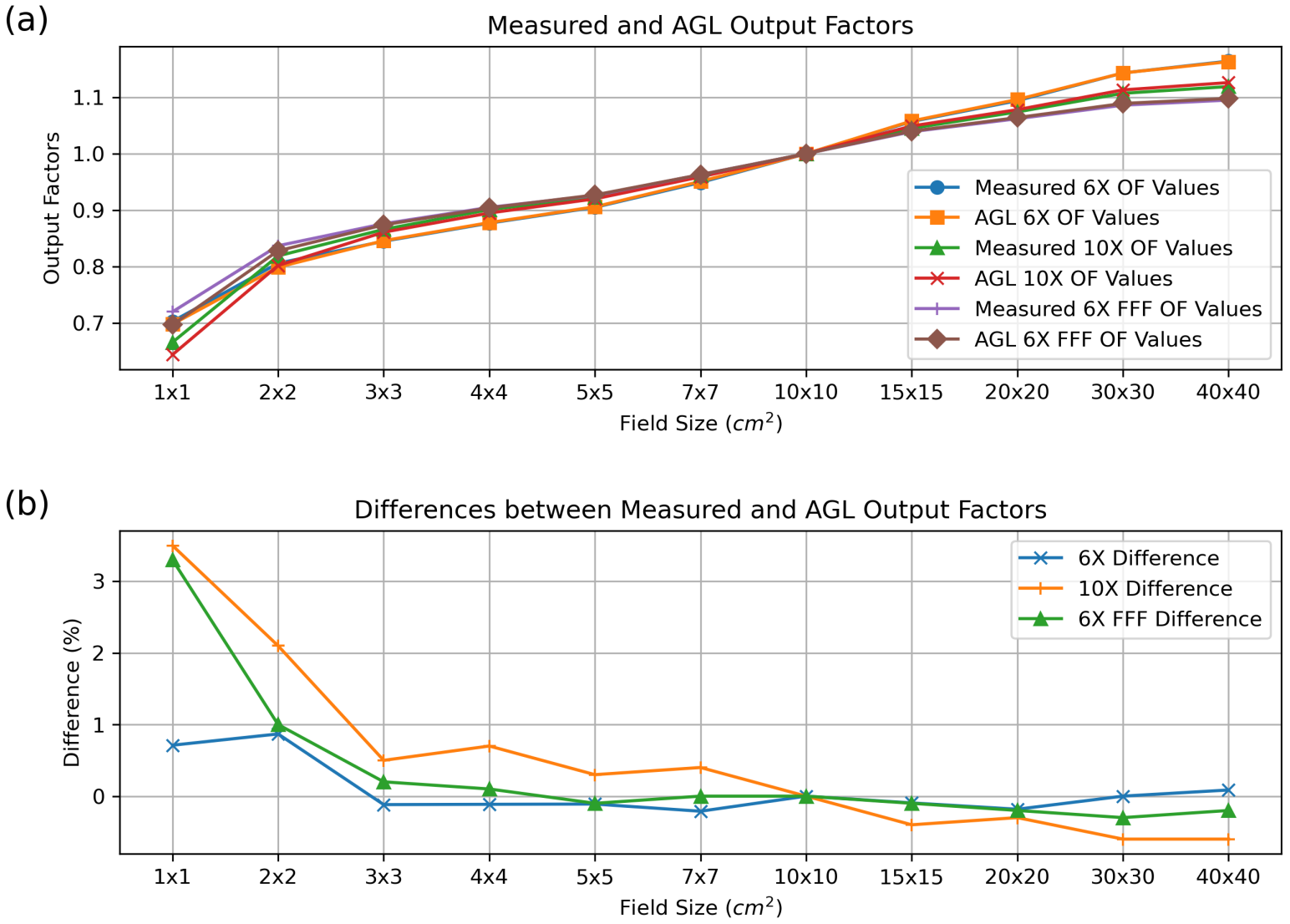


Figure 12: (a)Comparison of measured and AGL OFs for square FSs. (b) Difference between measured and AGL OF values.

4.2 CT to RED

Table 6 presents the density and mean HU values of various inserts within the CIRS M062 phantom, scanned on the Toshiba Aquillion LB CT scanner, as shown in the background of Figure 7, as well as scanned on the Siemens SOMATOM. Comparing the results with the CIRS Shane phantom, Figure 13 illustrates the close relation between the three data sets. However, a significant deviation is observed in the CT-ED curves from the Canon CT scanner at the lower HU range of -1000 HU to about -500 HU. This deviation at -1000 HU is potentially a result of miscalibration, as most CT scanners have two calibration points (air and water). Additionally, the large difference can be attributed to the different materials used for the inserts in these phantoms. The placement of lung inserts within the phantom is also a critical factor; nearby inserts of greater density can substantially affect RED measurements, primarily due to the phenomenon of beam hardening (Kitagawa et al., 2010). These differences can significantly impact dose computation by leading to inaccuracies in the calculated dose distribution, especially in low-density areas like lung tissue, potentially resulting in overestimation or underestimation of the dose. Miscalibration and different phantom materials can introduce errors, skewing dose calculations. Beam hardening can also distort RED measurements, causing artifacts and incorrect density readings. Consequently, dose computation may be inaccurate, impacting treatment planning and effectiveness. Ensuring accurate calibration and using appropriate materials in phantoms is essential for reliable dose calculations in clinical settings.

The comparison of CT-ED calibration curves for the CIRS M062 phantom on both the Canon and Siemens CT scanners showed a remarkable consistency, as illustrated in Figure 13. This suggests that the RED values derived from HU are comparable between the two systems, which implies that the scanners can be used interchangeably if the Canon CT is faulty or is under service, for treatment planning without significant discrepancies in dose calculations due to CT number variations.

Table 6: HU values obtained from scanning the CIRS M062 phantom with various RED inserts.

Material	Physical density	Density (10^{23})	REDw	HU		Average HU
Air	0	0	0	-983	-983	-983
Lung inhale	0.205	0.634	0.190	-763	-768	-765.5
Lung exhale	0.507	1.632	0.489	-486	-487	-486.5
adipose	0.96	3.171	0.949	-50	-50	-50
breast	0.99	3.261	0.976	-15	-12	-13.5
water	1	3.34	1	12	12	12
Liver	1.07	3.516	1.053	87	78	82.5
muscle	1.06	3.483	1.043	68	62	65
Bone 200	1.16	3.73	1.117	251	254	252.5
Bone 800	1.53	4.862	1.456	945	955	950
Bone 1250	1.82	5.663	1.696	1421	1421	1421

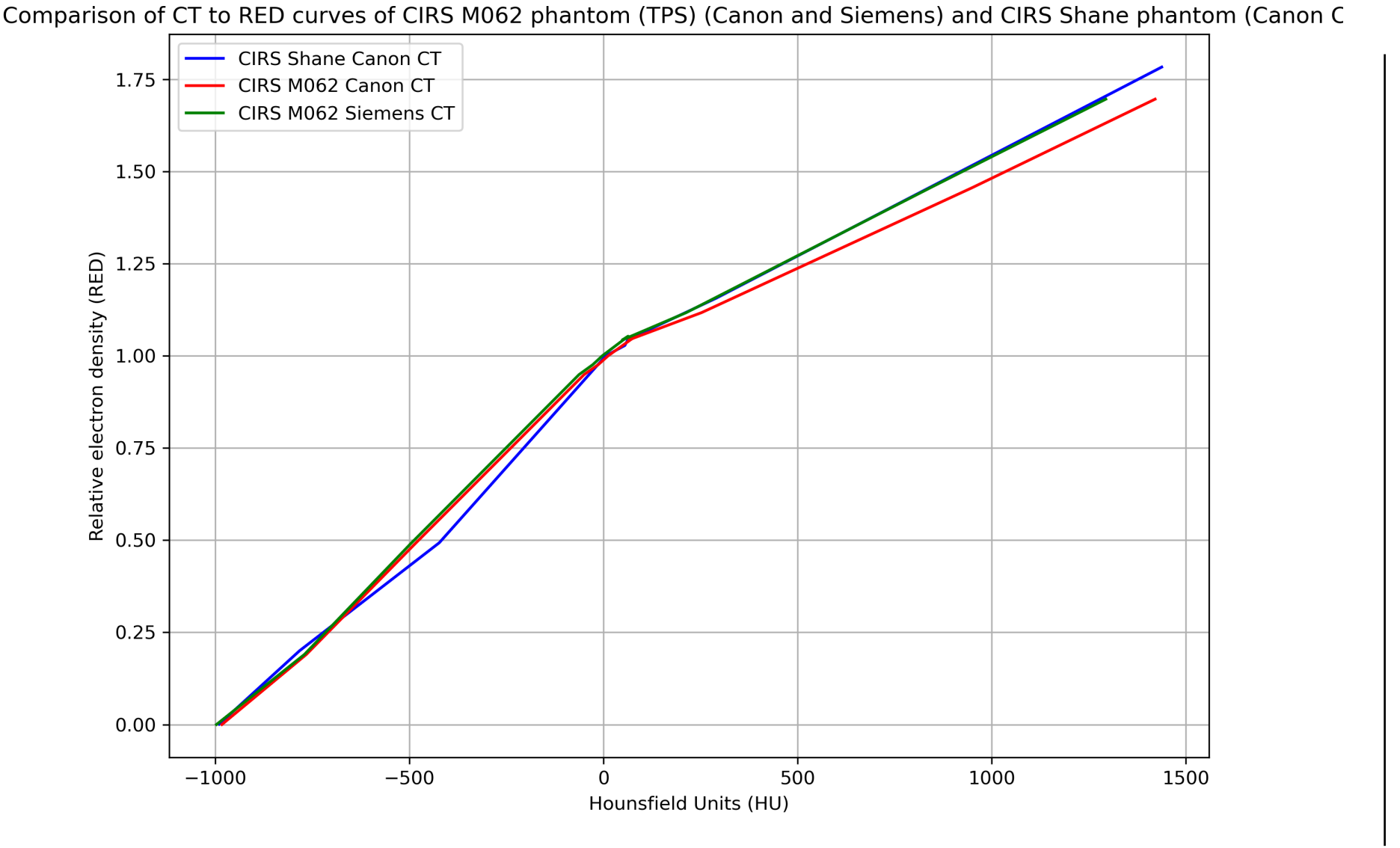


Figure 13: (a)Comparison of CT to RED curves measured with CIRS M062 phantom and CIRS SHANE phantom for the Canon Aquillion LB CT scanner. (b) Difference between CIRS M062 phantom and CIRS SHANE phantom RED values.

4.3 Beam modelling in Eclipse

The obtained data served as the input for the autofitting (Section 2.4.2) process in Eclipse, resulting in the creation of a beam model for Linac (Zhang et al., 2019). The most concerning PDDs and Profiles are shown below where the greatest difference between the measured and the modelled data for each energy was noticed.

Figure 14a illustrates a comparison of measured and modelled 6X photon beam profiles for an FS of $40 \times 40, \mathrm{cm}^2$ at a depth of 1.5 cm, highlighting the discrepancy between these two datasets. The noted differences, with a maximum difference of 10.9%, showcase one of the most significant variations encountered within the commissioning data between the measured and modelled values. This discrepancy is attributed to electron contamination at the shallow depth of measurement (Zhang et al., 2019).

Furthermore, Figures 14b and 14c detail the comparisons for the 6X FFF and 10X photon beams, respectively. For the 6X FFF beam with a FS of $35 \times 35, \mathrm{cm}^2$ at a depth of 1.8 cm, a difference of 9.4% was observed. Similarly, for the 10X beam with a FS of $30 \times 30, \mathrm{cm}^2$ at a depth of 1.5 cm, the error amounted to 9.3%. Similarly, the discrepancies were attributed to the electron contamination at the shallow measurement depths.

The disparities, as shown in Figures 14b and 14c, could stem from a range of factors as outlined by the IAEA (IAEA, 2017). These include differences in measurement versus calculation data due to the beam model fitting, the dose calculation algorithm, the verification measurement setup, and dosimeter measurement uncertainty. Some discrepancies may arise from systematic errors in the algorithms, while others may point to deficiencies across various stages of the treatment planning process. Notably, for both the 6X FFF beam at $35 \times 35, \mathrm{cm}^2$ FS and the 10X beam at $30 \times 30, \mathrm{cm}^2$ FS, difference in the penumbra region approached 9%, underscoring the impact of these factors on precision.

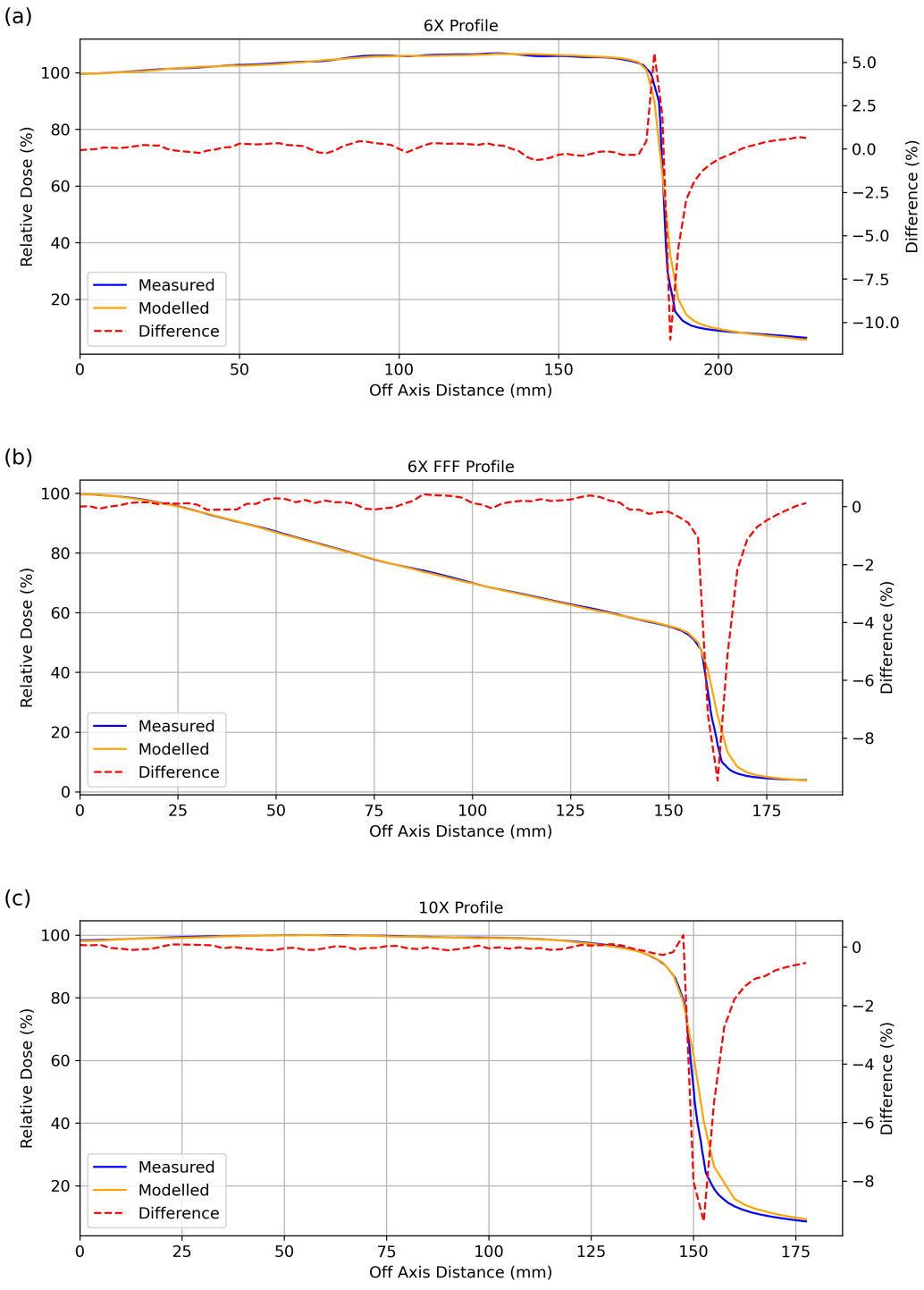


Figure 14: (a) Comparison of measured and modelled profiles for 6X, $40 \times 40, \mathrm{cm}^2$ at 1.5 cm depth, showing discrepancies. (b) Comparison of measured and modelled profiles for 6X, $35 \times 35, \mathrm{cm}^2$ at 1.8 cm depth, showing discrepancies. (c) Comparison of measured and modelled profiles for 10X, $30 \times 30, \mathrm{cm}^2$ at 1.5 cm depth, showing discrepancies.

Figure 15 depicts the difference between the measured and modelled PDD data for 6X, 6X FFF and 10X. Figure 15c shows the maximum difference of 7.3% between all of the measured and modelled PDD data. The main variation between the sets for all energies is found in the build-up region, which can also be attributed to the electron contamination of the beam.

Figure 16 presents the diagonal profiles for 6X, 6X FFF and 10 X photon beams, contrasting the measured and modelled outcomes for a larger FS of $40 \times 40, \mathrm{cm}^2$. While the discrepancy is substantially less in the central region of the fields, a substantial difference was noted in the penumbra regions for all energies with the greatest difference between the measured and modelled profiles being at 6X of 7.8% .

In all cases, slight disparities are observed in the build-up region for PDD curves and variations beyond the field edge for the profiles. The curves, depicted in red and blue, closely align, making it challenging to discern between the calculated and measured data, affirming the accuracy of the beam modelling. Generally, the PDDs and profiles modelled in Eclipse exhibit a minor relative dose difference of within 1.5% from the measurements with a maximum difference of 15% noted for smaller FSs. Other relative dose variations are observed throughout the profiles and PDDs but prominent in increasing/decreasing regions (build-up and penumbra), attributed to modelling/measurement inaccuracies.

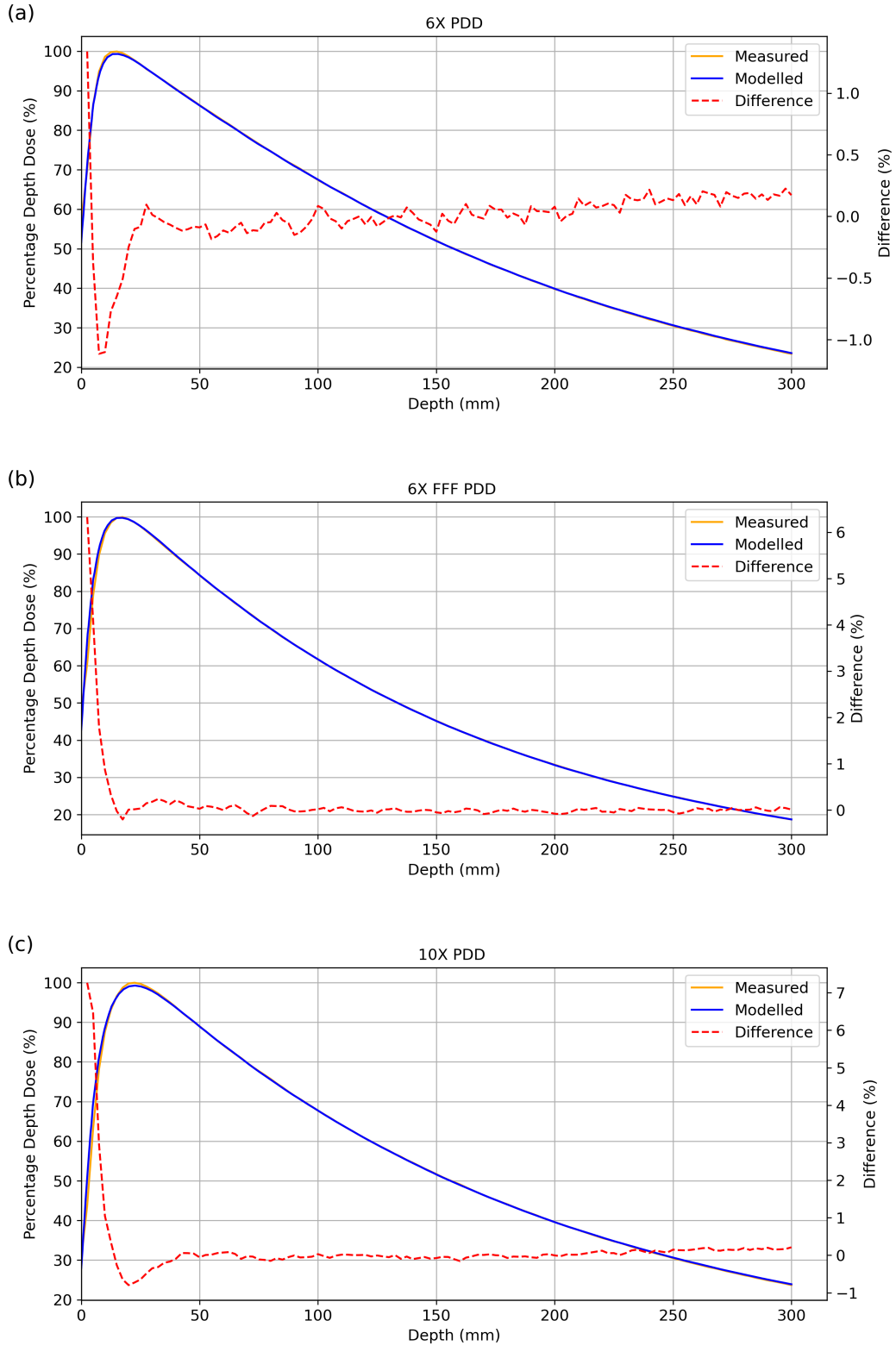


Figure 15: (a) Comparison of measured and modelled percentage depth dose for 6X, $15 \times 15\,\mathrm{cm}^2$, highlighting discrepancies. (b) Comparison of measured and modelled percentage depth dose for 6X FFF, $4 \times 4\,\mathrm{cm}^2$, highlighting discrepancies. (c) Comparison of measured and modelled percentage depth dose for 10X, $10 \times 10\,\mathrm{cm}^2$, highlighting discrepancies.

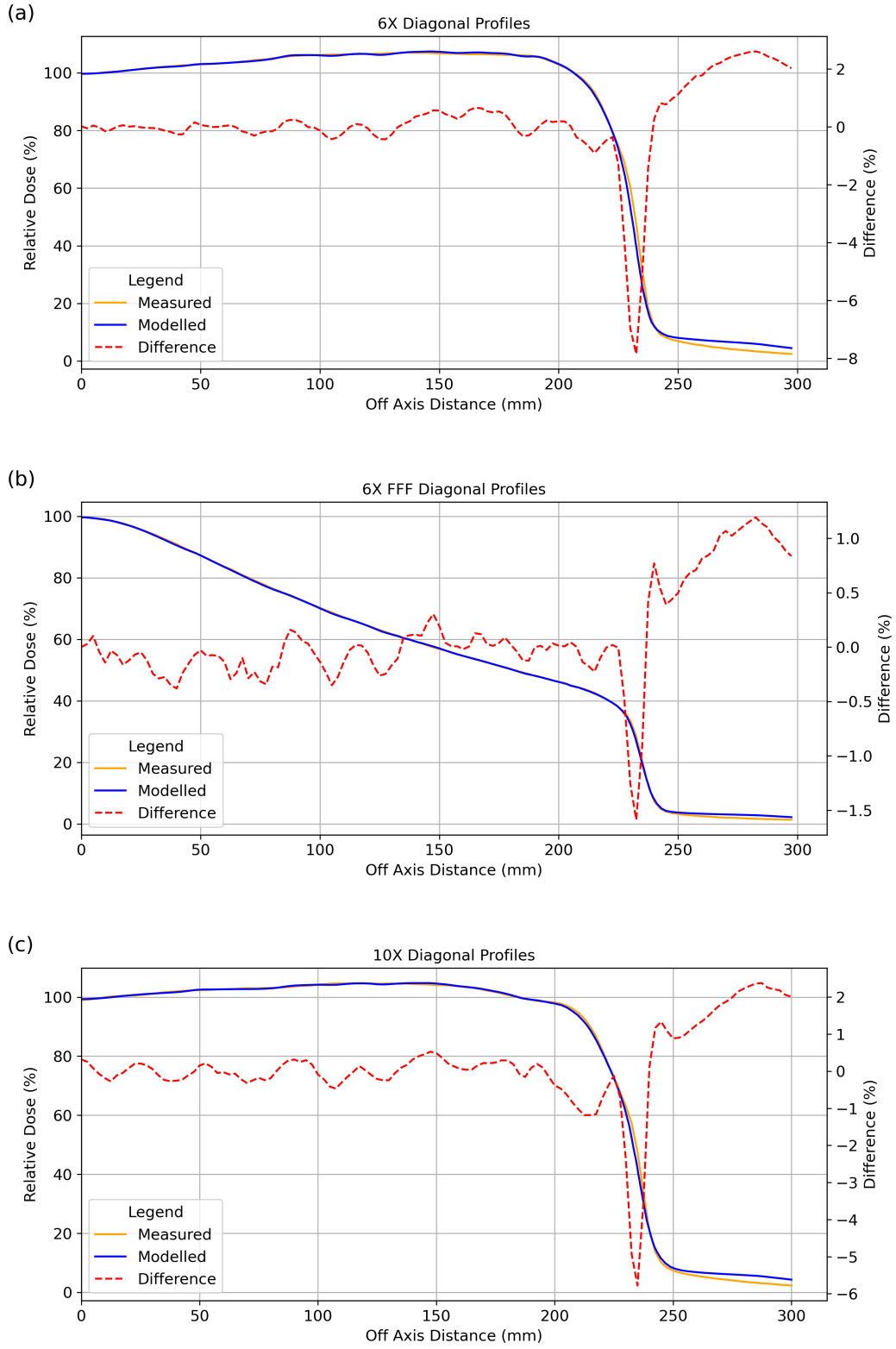


Figure 16: (a) Comparison of measured and modelled half diagonal profile for 6X beams at $40 \times 40\,\mathrm{cm}^2$ FS. (b) Comparison of measured and modelled half diagonal profile for 6X FFF beams at $40 \times 40\,\mathrm{cm}^2$ FS. (c) Comparison of measured and modelled half diagonal profile for 10X beams at $40 \times 40\,\mathrm{cm}^2$ FS.

4.4 DLG measurements

The MLC leaf transmission factors, highlighted in Table 7, showcased consistent results below the 0.5% threshold, aligning with previous studies and maintaining a margin below the AAPM Task Group No. 50's 2% threshold (Galvin et al., 1995) as well as in literature (Kong et al., 2015; Park et al., 2014). The DLG values obtained via the sweeping-gap method, as seen in Figure 17, are preliminary as they represent initial estimates before fine-tuning. This fine-tuning process, involving simulated patient plans, is aimed at refining these DLG estimates to achieve greater accuracy for the Eclipse TPS model, ensuring its clinical readiness and adherence to the high precision required for patient treatments. The detailed optimisation in Section 4.5 moves beyond these initial DLG estimates, adjusting them based on clinical plan simulations.

This technique progressively narrowed the gap sizes and recorded the ionisation chamber readings after making necessary corrections, including adjusting MLC leaf transmission observed with closed leaves. As illustrated in Figure 17, a linear fitting method was employed to estimate a theoretical negative gap size that would bring the ionisation chamber readings down to zero. The absolute magnitude of this negative gap is indicative of the DLG, which measures the leaf end transmission with closed leaves, providing a preliminary set of DLG values.

Table 7: Measured DLG and MLC transmission.

	DLG (mm)	MLC transmission
6X	0.31	0.44%
10X	0.47	0.45%
6X FFF	0.38	0.29%

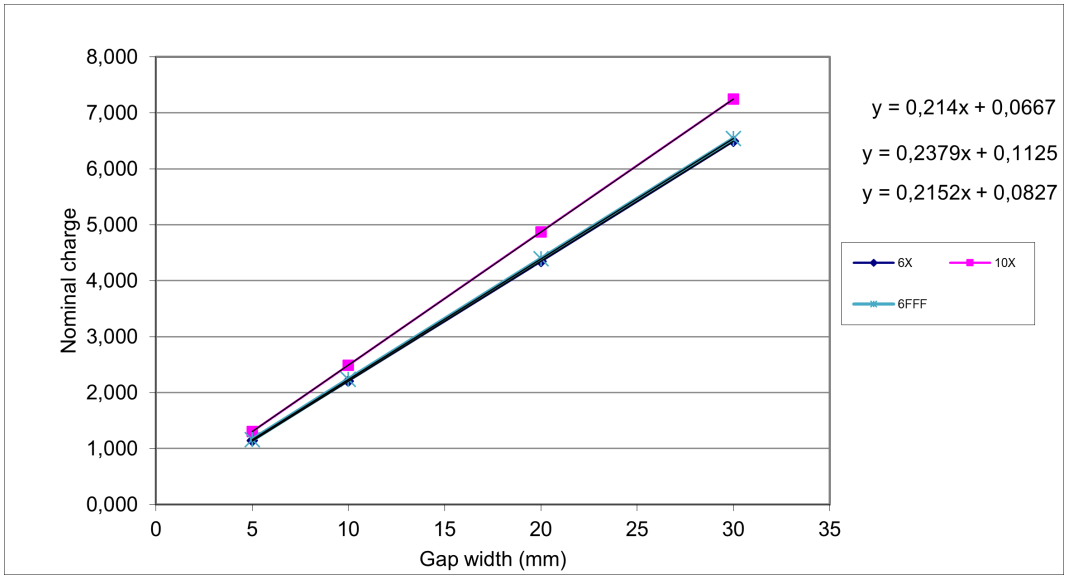


Figure 17: The measurement of DLG, using the sweeping-gap technique as a modelling factor for MLC leaf end transmission, reveals a linear relationship in the data. This analysis produced initial DLG values specific to each energy: 0.21 mm (6X), 0.22 mm (6X FFF), and 0.24 mm (10X).

4.5 Comprehensive Dosimetric Validation and Quality Assurance of Beam Models

Reference dosimetry for each energy was conducted in accordance with the IAEA TRS-398 protocol (IAEA, 2001) to verify the proper calibration of the Linacs, using an independent PTW Semiflex 0.125 cc chamber for dose measurements. The calibration checks were conducted in a PTW BeamScan water tank, under reference conditions (SSD = 100 cm, depth 10 cm, FS $10 \times 10\,\mathrm{cm}^2$). The charge collected for 100 MU was converted to dose, applying correction factors as stated in TRS 398 (IAEA, 2001). As detailed in Table 8, the measurement results confirmed that the Linacs were calibrated to deliver the correct pre-determined doses. The measured doses closely matched the expected values, with deviations within acceptable limits, thereby ensuring the accuracy and reliability of the Linac systems in clinical settings.

Inter-comparisons with a PTW Farmer 0.6 cc chamber showed differences

within 0.5% for all energies. Despite a 2% difference between evening and morning measurements, values stayed within the South African Standards for Quality Assurance in Radiotherapy (SASQART) output tolerance of ±2%, negating the need for calibration adjustments.

Table 8: Reference dosimetry results using an independent chamber.

Energy	**Expected Dose (Gy)**	**Measured Dose(Gy)**	**Difference (%)**
6X	1.0000	1.0018	-0.18
10X	1.0000	1.0164	-1.64
6X FFF	1.0000	1.0260	-2.60

The original four field plans described in Section 3.4.2, calculated on the test unit, point dose results are presented in Table 9. These results illustrated two important points. The first was the successful transfer of the different beam parameters from the TPS to Mosaiq, ensuring the correct couch, collimator and gantry orientation were used with regard to the convention scales (IEC 61217). Secondly, the differences between the calculated and measured doses were within 3% as set out by Venselaar and Welleweerd (Venselaar and Welleweerd, 2001) and indicated that the AAA algorithm functioned correctly.

Table 10 illustrates the difference between the measured point dose for different treatment areas and the point dose measurements using a PTW Semiflex 0.125 cc chamber mentioned in Table 4. These results were within the 3% tolerance and showcased the correct calculation when more advanced plans were applied to the RW3 solid water phantom.

Once the point dose measurements were completed and the results cross-checked with the calculated values, the same plans were transferred to the Octavius 4D CT data set. Both the head and neck, as well as the prostate beams for each energy were applied to the CT data set, and the dose distribution was determined. In preparation for the plans to be delivered on the PTW Octavius 4D phantom, three cross-calibration plans, one for each energy were created on Eclipse. These plans consisted of a standard $10 \times 10\,\mathrm{cm}^2$

Table 9: Comparison of initial measured and calculated doses using AAA algorithm on the test server for the four field plans (Beam parameters indicated below each energy) on a RW3 slab phantom. The results were normalised to a $10 \times 10\,cm^2$ field delivering 1 Gy to isocentre at SSD=95 cm, depth 5 cm.

6X	**Dose Calculated (Gy)**	**Dose Measured (Gy)**	**Difference**
Gantry 20°, Couch 90°, Table 0°, Coll 0°, $10 \times 10\,cm^2$	2.006	2.003	0.1%
Gantry 90°, Couch 0°, Table 0°, Coll 330°, $5 \times 20\,cm^2$	1.975	1.999	-1.2%
Gantry 180°, Couch 0°, Table 0°, Coll 330°, $20 \times 20\,cm^2$	2.009	1.997	0.6%
Gantry 270°, Couch 0°, Table 0°, Coll 330°, $3 \times 3\,cm^2$	1.985	2.001	-0.8%
6X FFF	**Dose Calculated (Gy)**	**Dose Measured (Gy)**	**Difference**
Gantry 20°, Couch 90°, Table 0°, Coll 0°, $10 \times 10\,cm^2$	2.013	1.988	1.3%
Gantry 90°, Couch 0°, Table 0°, Coll 330°, $5 \times 20\,cm^2$	2.013	1.983	1.5%
Gantry 180°, Couch 0°, Table 0°, Coll 330°, $20 \times 20\,cm^2$	2.016	2.012	0.2%
Gantry 270°, Couch 0°, Table 0°, Coll 330°, $3 \times 3\,cm^2$	1.997	2.018	-1.0%
10X	**Dose Calculated (Gy)**	**Dose Measured (Gy)**	**Difference**
Gantry 20°, Couch 90°, Table 0°, Coll 0°, $10 \times 10\,cm^2$	2.005	2.017	-0.60%
Gantry 90°, Couch 0°, Table 0°, Coll 330°, $5 \times 20\,cm^2$	2.006	1.985	1.1%
Gantry 180°, Couch 0°, Table 0°, Coll 330°, $20 \times 20\,cm^2$	2.017	1.984	1.7%
Gantry 270°, Couch 0°, Table 0°, Coll 330°, $3 \times 3\,cm^2$	1.972	2.012	-2.0%

Table 10: Point dose measurements in the RW3 slab phantom at the isocentre location for VMAT plans calculated using AAA algorithm on the test server.

6X	**Dose Calculated (Gy)**	**Dose Measured (Gy)**	**Difference (%)**
Head and Neck VMAT	1.651	1.649	0.1
Prostate VMAT	2.336	2.381	-1.9
6X FFF	**Dose Calculated (Gy)**	**Dose Measured (Gy)**	**Difference (%)**
Head and Neck VMAT	1.658	1.659	-0.1
Prostate VMAT	2.382	2.418	-1.5
10X	**Dose Calculated (Gy)**	**Dose Measured (Gy)**	**Difference (%)**
Head and Neck VMAT	1.817	1.821	-0.2
Prostate VMAT	2.609	2.656	-1.8

FS, delivering 1 Gy to the detector surface on the 2D array as per PTWs recommendation.

Once the cross-calibration correction factor for an energy was applied, the plans were re-treated on the phantom and the dose distribution was measured on the 2D array. The results were compared to the calculated distribution through the PTW Verisoft software, and as mentioned in Section 2.4.3, a volumetric gamma analysis was performed. The results of each of these plans were used iteratively to optimize the DLG and MLC transmission factors until the highest possible pass rates were achieved. The final MLC transmission and DLG values used in the beam model are shown in Table 11.

Table 11: DLG and MLC transmission values used in the beam model.

	DLG (mm)	MLC transmission
6X	0,02	0,15%
10X	0,027	0,15%
6X FFF	0,02	0,15%

It is noteworthy that the MLC transmission values for all beam energies (6X, 10X, and 6X FFF) were standardized to 0.15% in the final beam model. Ini-

tially, as shown in Table 7, the measured MLC transmission values were different for each energy, with variations ranging from 0.29% to 0.45%. Additionally, the final chosen value of 0.15% represents a compromise that closely approximates the actual transmission characteristics while maintaining consistency and reliability in the dose distribution results. This approach helps in minimizing discrepancies that could arise from slight variations in MLC transmission, which might not significantly impact clinical outcomes but could complicate the optimization process.

Complying with the IAEA audit methodology, Tables 12 to 14 show the comparison between the calculated point doses for the different chamber positions and the respective measured point doses. A tolerance of 5% was applied to all the PTV volumes and a 7% was applied for the spinal cord volume. In each case the difference between the calculated and measured doses, fell within the limits set out above for all energies.

Table 12: Comparison of initial measured and calculated doses using AAA algorithm for CIRS Shane phantom for 6X.

Volume	Structure associated with position of chamber	TPS calculated mean dose (Gy)	Mean measured dose (Gy)	Difference (%)
IC_PTV_7000	PTV_7000 (nasopharynx), isocentre, red channel no 1	2.329	2.404	-3.1
IC_PTVn1_6000	PTVn1_6000 (involved nodes), 5 cm inferior to isocentre, blue channel no 2	2.054	2.092	-1.8
IC_PTVn2_5400	PTVn2_5400 (elective nodes), 5 cm inferior to isocentre, blue channel no 3	1.891	1.954	-3.2
IC_SpinalCord	IC_SpinalCord, 5 cm inferior to isocentre, blue channel no 4	1.141	1.14	0.1

Table 13: Comparison of initial measured and calculated doses using AAA algorithm for CIRS Shane phantom for 6X FFF.

Volume	Structure associated with position of chamber	TPS calculated mean dose (Gy)	Mean measured dose (Gy)	Difference (%)
IC_PTV_7000	PTV_7000 (nasopharynx), isocentre, red channel no 1	2.353	2.419	-2.7
IC_PTVn1_6000	PTVn1_6000 (involved nodes), 5 cm inferior to isocentre, blue channel no 2	1.782	1.732	2.9
IC_PTVn2_5400	PTVn2_5400 (elective nodes), 5 cm inferior to isocentre, blue channel no 3	1.641	1.646	-0.3
IC_SpinalCord	IC_SpinalCord, 5 cm inferior to isocentre, blue channel no 4	0.966	0.924	4.5

Table 14: Comparison of initial measured and calculated doses using AAA algorithm for CIRS Shane phantom for 10X.

Volume	Structure associated with position of chamber	TPS calculated mean dose (Gy)	Mean measured dose (Gy)	Difference (%)
IC_PTV_7000	PTV_7000 (nasopharynx), isocentre, red channel no 1	2.329	2.404	-3.1
IC_PTVn1_6000	PTVn1_6000 (involved nodes), 5 cm inferior to isocentre, blue channel no 2	2.054	2.092	-1.8
IC_PTVn2_5400	PTVn2_5400 (elective nodes), 5 cm inferior to isocentre, blue channel no 3	1.891	1.954	-3.2
IC_SpinalCord	IC_SpinalCord, 5 cm inferior to isocentre, blue channel no 4	1.141	1.14	0.1

As part of the final step in the dosimetric validation, patient-specific quality assurance (PSQA), using the PTW Octavius 4D phantom, was done for the head and neck, and prostate plans. The plans were analysed according to the protocol of TG 218 (Miften et al., 2018). A DTA of 2 mm, DD of 3 % and a dose suppression of 10 % below the normalisation of the measured dose distribution with acceptable passing criteria of $\geq 95\%$. The results for each of the plans at different energies are shown below in Table 15. As per the above criteria, all plans for all energies passed and the test server TPS was accepted.

Table 15: Patient-Specific Quality Assurance results for each test plan with DTA of2mm and DD 5%

	Results		
Plan	**6X (%)**	**10X (%)**	**6X FFF (%)**
H&N VMAT	97.5	97.3	98.4
Prostate VMAT	98.6	98.3	97.6

4.6 Implementation and Challenges of a Collaborative Off-site Treatment Planning Services

The final workflow was specifically designed to clarify the roles and responsibilities of all parties: Medical Physicists, Radiotherapists, Radiation Oncologists, and External Treatment Planners.

4.6.1 Workflow Implemented

The integration of external treatment planning services provided by Varian represents an alternative model in the radiotherapy workflow at CMJAH. This service leverages a blend of advanced technologies and robust security measures to ensure seamless, efficient, and secure treatment planning processes.

The workflow initiates with a Planning CT Scan conducted by the local Radiotherapists at CMJAH's CT scanner facility, where every patient is meticulously informed of their participation in a pilot study. Before the scan, patients are required to sign a consent form to inform them about the study details and obtain their explicit consent to be a part of this innovative research initiative.

The acquired CT data is seamlessly transferred to the Siemens Healthineers server, located alongside the main TPS server. The server anonymizes the CT data, uploads it to the Siemens Healthineers RadAI cloud-based contouring system, and then contours it. The contoured data is then re-downloaded to the server, un-anonymized, and sent to the TPS system.

Through a secure virtual private network (VPN) service, Varian's remote treatment planners can connect to the TPS server housed at CMJAH, ensuring a protected and consistent link between their workstations and the hospital server. In strict adherence to the POPIA, which safeguards patient information, all patient data is handled with the utmost confidentiality and remains exclusively on the CMJAH server. There is no provision for downloading onto individual workstations, thus maintaining the highest standards of data security.

The remote planners import the CT dataset and the AI-generated contoured structure set into the Eclipse TPS. They meticulously verify the completeness and accuracy of the data, ensuring that all required structures have been contoured by the AI software. Following this, the radiation oncologist at CMJAH is informed to review and validate the contours and to define the treatment volumes.

Upon clearance from the Radiation Oncologist, Varian's remote planners proceeded to create the treatment plan, adhering strictly to the clinical protocols prescribed by CMJAH. Upon completion, the plan is presented to the Medical Physicist at CMJAH for a thorough physics check—this step acts as a critical quality assurance measure, validating the plan's integrity and safety.

When the Medical Physicist expresses satisfaction with the plan, it is then forwarded for final review and approval by the consulting physician. Approved plans are subjected to PSQA using the Octavius 4D phantom, which is a standard practice to guarantee the plan's efficacy. If the plan passes the PSQA criteria, it receives the final nod for treatment, and the patient's treatment sessions are scheduled accordingly.

Throughout this workflow, the local radiotherapy team at CMJAH plays an instrumental role, performing checks parallel to those for an in-house Monaco plan. This involvement ensures that patient care is maintained and that every phase of the workflow receives the necessary attention.

The accompanying proposed workflow diagram (Figure 18) offers a visual representation of this intricate process, from the initial planning stages through to the final treatment approval. It encapsulates the various checkpoints, approvals, and collaborative interactions that define the modern radiotherapy planning and delivery process at CMJAH.

4.6.2 Test patients results

Five mock patients were planned using the remote infrastructure to ensure the seamless operation of the complete OTPS. This exercise was crucial for

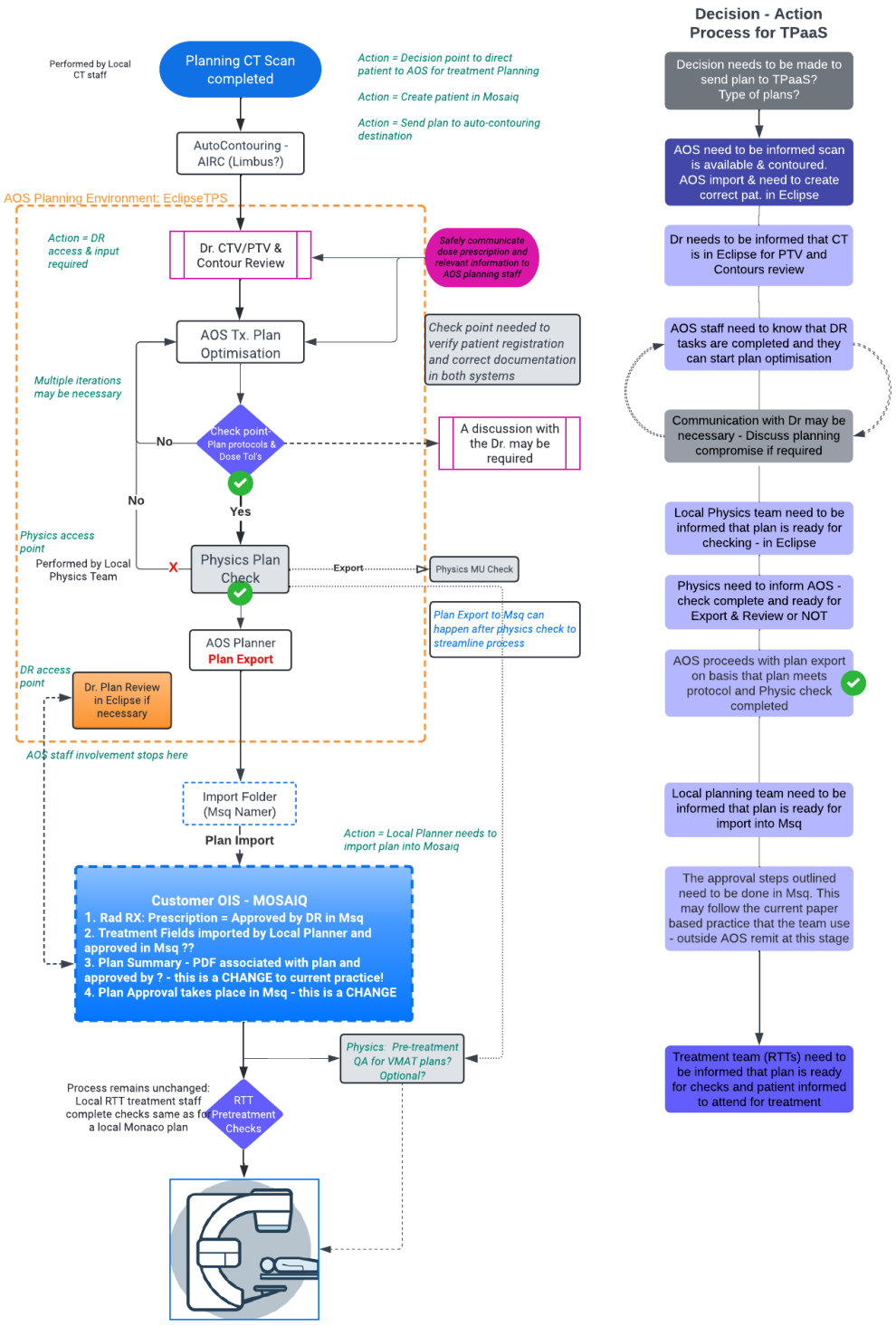


Figure 18: Final Workflow implemented at CMJAH for OTPS provided by Niall M^{c}Andrew (Varian).

verifying the system's and software's integrated functionality, serving as the final validation step before clinical deployment. The mock plans underwent the same patient-specific procedures described previously. In the analysis of the files, a DTA of 3 mm, DD of 3%, and a dose suppression of 5% below the normalization of the measured dose distribution were used. This criteria (different from TG 218) was less stringent than the criteria used in Section 4.5. This was because the criteria utilized in this analysis are consistent with those used in the clinical setting at CMJAH for the evaluation of patient data. The results of the mock patients are shown in Table 16. It should be noted that no specific energy was used throughout the plans, but it varied according to the protocols set out by the CMJAH radiation oncology department.

Table 16: Patient-Specific Quality Assurance results for the five mock patients with DTA of 3 mm and DD 3%

Patient	**Location**	**Results (%)**
VarianTest 1	Prostate	98.90
VarianTest 2	Head and Neck	91.90
VarianTest 3	Breast	97.50
VarianTest 4	Prostate	99.20
VarianTest 5	Breast	98.80

As all results were above the 90% action limit set out by TG 218 (Miften et al., 2018), the final approval was given from the relevant stakeholders at CMJAH and Varian that the system was to be used for the final test run of 100 patients.

4.6.3 Feasibility of OTPS

The integration of off-site treatment planning services at CMJAH represents a pioneering approach to addressing the multifaceted challenges of radiation therapy delivery. This innovative model, leveraging AI for contouring and remote planning capabilities, has not only streamlined the treatment planning process but also substantially mitigated the impact of local staff shortages.

By allocating resources more efficiently, the hospital has been able to focus on clearing treatment backlogs, particularly in critical care areas, thereby improving patient care delivery and outcomes.

One of the system's significant advantages is AI-driven contouring, which has markedly reduced the time physicians spend on manual contouring tasks, as demonstrated by Doolan et al. (Doolan et al., 2023). This efficiency gain allows doctors to dedicate more attention to patient care and treatment strategy, enhancing the quality of service. Furthermore, the flexibility offered by off-site planners introduces a new level of adaptability in managing workload fluctuations. This elasticity is vital for institutions grappling with variable patient volumes and staffing levels, ensuring that treatment quality and timeliness remain uncompromised.

Moreover, the system's robustness was evident in the seamless coordination between different service components—ranging from patient scanning, RadAI contouring software, prescription by doctors, planning by off-site planners, to checks by physics and local radiotherapists. This coordinated effort underscores the system's operational viability and sets a precedent for future implementations. The ability to maintain high treatment standards while navigating the challenges of remote coordination speaks volumes about the system's feasibility and potential as a scalable solution for radiation therapy services.

4.6.4 Implementation Challenges

Integrating off-site treatment planning services introduced significant challenges, necessitating proper communication across a multidisciplinary team. This required coordinating with engineers to seamlessly integrate the CT scanner, AI contouring system, Eclipse, and Monaco TPS systems, alongside local IT support. The complexity of setting up remote access/VPN systems further extended setup times, leading to the expiration of trial licenses for critical software like the Eclipse TPS and AI contouring software. Addressing these issues demanded obtaining special permissions to reinstate these licenses, crucial for

maintaining the study's continuity.

Implementation challenges also encompassed adjusting roles and responsibilities, notably suggesting that radiotherapists at CMJAH assume more central roles in printing, exporting, and preparing for treatment. This strategy aimed to enhance workflow efficiency by fostering a sense of ownership among radiotherapists, ensuring they are well-acquainted with treatment plans to address any arising issues confidently. However, this required radiotherapists to have access to the Eclipse treatment planning system, altering the traditional responsibilities away from the physics team, who would no longer engage in printing, exporting, or performing pre-treatment checks before exporting the plans to Mosaiq.

These workflow adjustments encountered obstacles, especially due to using Mosaiq R&V system instead of Eclipse's ARIA R&V, presenting challenges for local radiotherapists in adapting to the new workflow. Radiotherapists faced difficulties in accepting treatment plans, receiving only beam summary reports from Eclipse without direct access to the treatment plans. Despite all plans passing checks and meeting dosimetric criteria, the lack of visibility into detailed plans caused unease. The introduction of radiotherapists' roles in entering or verifying treatment parameters in the R&V system, as mandated by radiation safety standards and regulatory guidelines (Washington and Leaver, 2015; Pawlicki et al., 2011), underscores the importance of ensuring treatment delivery aligns with planned parameters, maintaining records for audits and compliance. This situation underscores the necessity for clear communication, thorough training, and ensuring system compatibility to facilitate a smooth transition and broader acceptance of innovative treatment planning and delivery processes.

4.6.5 Future research

Due to lack of quantitative data regarding the impact of the OTPS on treatment planning accuracy, efficiency, and patient throughput, the following areas

are suggested for future research:

1. Simulation-to-Treatment Time Analysis:

   Future studies should measure the time from patient simulation to the start of treatment. By comparing this before and after OTPS implementation, researchers can evaluate improvements in efficiency and patient throughput.

2. Accuracy of Treatment Plans:

   Research should compare dosimetric parameters between plans developed on-site and those developed remotely. Metrics such as dose distribution, conformity indices, and organ-at-risk sparing should be analyzed to assess accuracy.

3. Impact on Cancer Treatment Backlog:

   A longitudinal study tracking patient volumes, wait times, and throughput before and after OTPS implementation is recommended. This data will help quantify the system's effectiveness in reducing the backlog and improving access to treatment.

4. Quality Assurance Metrics:

   Future research should focus on establishing comprehensive QA metrics specific to OTPS. This includes regular assessment of plan verification accuracy, equipment calibration consistency, and error rates.

5 Conclusion

The comprehensive evaluation of the Eclipse system and Elekta VersaHD Linacs commissioning process has provided critical insights, confirming both the precision of beam modelling and the viability of remote treatment planning. This study meticulously gathered a broad spectrum of data, including profiles, PDDs, and OFs, crucial for the exact modelling required for effective and reliable treatment planning.

In detailing the commissioning process, the study highlights the beam data collection, such as the PDD measurements for 6X, 10X, and 6X FFF photons with FSs varying between $1 \times 1, \mathrm{cm}^2$ to $40 \times 40, \mathrm{cm}^2$ and profiles for FSs $1 \times 1, \mathrm{cm}^2$ to $40 \times 40, \mathrm{cm}^2$ at varying depths. Notable findings include deviations between measured and Accelerated Go Live (AGL) OFs for 10X and 6X FFF, with discrepancies of 3.3% and 3.5% respectively, underscoring the need for greater accuracy when dealing with small FSs as stated in TRS-483 (Palmans et al., 2018). The CT to Electron Density comparison between the CIRS M062 and CIRS Shane phantom revealed the most deviation in the lower HU range of -1000 HU to about -500 HU. This variance is potentially due to miscalibration, as most CT scanners have two calibration points (air and water). Additionally, it is attributed to the use of different materials for phantom inserts and their critical placement.

The Eclipse beam modelling process unveiled deviations, notably a 14.5% discrepancy in 6X photon profiles for a $4 \times 4\,\mathrm{cm}^2$ FS. This phase of dosimetric validation confirmed the Linacs' calibration accuracy, with measured doses closely aligning with expected values and inter-comparisons between CMJAH ionisation chambers and independently calibrated ionisation chambers showing minimal differences across all energies. Moreover, PSQA outcomes for head and neck and prostate plans exceeded action level criteria of TG 218 (Miften et al., 2018), achieving passing rates above 90% for DTA of 3 mm and DD of 3%, thereby affirming the AAA clinical implementation's success.

The results from the five mock patients not only demonstrate the technical feasibility but also the practical application of the commissioned system for OTPS. The successful commissioning, marked by dosimetric validation and adherence to quality assurance standards, lays a solid foundation for remotely extending radiation therapy services. It highlights the potential to improve treatment planning flexibility, resource utilisation, and ultimately patient outcomes by leveraging sophisticated TPSs in conjunction with meticulously commissioned Linacs.

However, it is essential to distinguish the commissioning process's technical success from the broader operational feasibility of implementing remote services. While technical precision and system validation are foundational, the operational feasibility of OTPS at CMJAH has been underscored by its ability to address challenges such as staff shortages and treatment backlogs, improving patient care delivery and outcomes. The OTPS model's success in streamlining the treatment planning process through AI-driven contouring and remote planning, alongside its ability to overcome implementation challenges such as integrating complex systems and adapting workflows, highlights a comprehensive approach to enhancing radiation therapy services. Yet, the distinction between technical commissioning and the holistic operational implementation of OTPS emphasises the need for careful consideration of all facets, including system compatibility, communication, training, and workflow adjustments, to fully realize the potential of remote treatment planning services.

This understanding reaffirms the report's conclusion that while the integration of the Varian Eclipse TPS with Elekta Linacs for remote treatment planning services has been technically validated, the operational deployment of such services must carefully navigate the complexities of integrating new technologies into established healthcare environments to enhance treatment planning efficiency and patient care.

References

A prospective study on the impact of waiting times for radiotherapy for cervical cancer at harlotte Maxeke Johannesburg Academic Hospital, South Africa, author = Lohlun, K. N. and Kotzen, J. and Lakier, R., journal = South African Journal of Gynaecological Oncology, volume = 7, number = 2, pages = 4-8, year = 2015, doi = 10.7196/SAJOG.985.

Peter R. Almond, Paul J. Biggs, Bert M. Coursey, William F. Hanson, M. Saiful Huq, Ravinder Nath, and David W. O. Rogers. Accelerator beam data commissioning equipment and procedures: Report of the TG-106 of the therapy physics committee of the aapm. Report TG 106, American Association of Physicists in Medicine, 2008.

P. Andreo, J. Cramb, B.A. Fraass, F. Ionescu-Farca, J. Izewska, V. Levin, B. Mijnheer, J.-C. Rosenwald, P. Scalliet, K.R. Shortt, J. Van Dyk, and S. Vatnitsky. Commissioning and quality assurance of computerized planning systems for radiation treatment of cancer. Technical Report 430, International Atomic Energy Agency, 2004.

A. Belard, D. Dolney, T. Zelig, J. E. McDonough, and J. O'Connell. Improving proton therapy accessibility through seamless electronic integration of remote treatment planning sites. *Telemedicine and E-Health*, 17:370–375, 2011. doi: 10.1089/tmj.2010.0199.

M. Bhagwat, Z. Han, S. Ng, and P. Zygmanski. An oscillating sweeping gap test for VMAT quality assurance. *Physics in Medicine & Biology*, 55(17), 2010.

A. Boyer, P. Biggs, J. Galvin, E. Klein, T. LoSasso, D. Low, K. Mah, and C. Yu. AAPM Report no. 72: Basic applications of multileaf collimators, report of task group no. 50 radiation therapy committee. *Madison, WI: aapm*, 2001.

B. A. Brevitt, E. G. Suarez, R. A. M. Clemente, and M. Voutchkov. Evaluating

the impact of CT scanning parameters on dose calculations by the treatment planning system in external beam radiation therapy. *Journal of Cancer Therapy and Research*, 1, 2021.

E. Brunckhorst, E. Gershkevitsh, G. Ibbott, G. Korf, D. Miller, R. Schmidt, J. Van Dyk, G. Velez, J. Welleweerd, S. Wanwilairat, F. Yip, and S. Vatnitsky. Commissioning of radiotherapy treatment planning systems: Testing for typical external beam treatment techniques. Technical Report 1583, International Atomic Energy Agency, Vienna, 2008.

I. Chauvet, A. Petitfils, C. Lehobey, J. Y. Kristner, Y. Brunet, R. Lembrez, G. Gaboriaud, A. Mazal, S. Zefkili, and J. C. Rosenwald. The sliding slit test for dynamic IMRT: a useful tool for adjustment of mlc related parameters. *Physics in Medicine and Biology*, 50(4):563–580, 2005.

S. Chen, B. Y. Yi, X. Yang, H. Xu, K. L. Prado, and W. D. D'Souza. Optimizing the mlc model parameters for imrt in the raystation treatment planning system. *Journal of Applied Clinical Medical Physics*, 16(5):322–332, 2015. doi: 10.1120/jacmp.v16i5.5548.

Wen-Zhou Chen. Impact of dose calculation algorithm on radiation therapy. *World Journal of Radiology*, 6(11):874, 2014.

B. S. Chera, L. Potters, and L. B. Marks. Restructuring our approach to peer review: A critical need to improve the quality and safety of radiation therapy. *Practical Radiation Oncology*, 10:321–323, 2020. doi: 10.1016/j.pro.2020.07.001.

Ivan Ciancaglioni, Marco Marinelli, Enrico Milani, Giancarlo Prestopino, Claudio Verona, Gianluca Verona-Rinati, Roberto Consorti, Alessio Petrucci, and Francesco De Notaristefani. Dosimetric characterization of a synthetic single crystal diamond detector in clinical radiation therapy small photon beams. *Medical Physics*, 39(7):4493–4501, 2012. doi: 10.1118/1.4729739.

Catharine Clark, Eduard Gershkevitsh, Wolfgang Lechner, Jake Van Dyk, Daniel Venencia, Tomislav Bokulic, Pavel Kazantsev, and Paulina

Wesolowska. National "End-to-End" Audit Programme for dose delivery using intensity-modulated radiation therapy through on-site visits to radiation therapy institutions. Technical report, International Atomic Energy Agency, Vienna, Austria, 2019.

D. Cutright, M. Gopalakrishnan, V. Sathiaseelan, and R. Lurie. SU-E-T-261: Dosimetric characterization and comparison of the Elekta Agility and mlci2 Multi-Leaf Collimator Heads. *Medical Physics*, 40:264–264, 2013. doi: 10.1118/1.4814696.

Daily Maverick. Gauteng health's silence on R784m oncology backlog tender is worrying: Cancer alliance. *Daily Maverick*, January 2024. URL `https://www.dailymaverick.co.za/article/2024-01-25-gauteng-healths-silence-on-r784m-oncology-backlog-tender-is-worrying-cancer-alliance/`.

I. Das, C. Cheng, R. Watts, A. Ahnesjö, J. Gibbons, X. Li, J. Lowenstein, R. Mitra, W. Simon, and T. Zhu. Accelerator beam data commissioning equipment and procedures: Report of the TG-106 of the therapy physics committee of the aapm. *Medical Physics*, 35:4186–4215, 2008.

I. J. Das, C. F. Njeh, and C. G. Orton. Vendor provided machine data should never be used as a substitute for fully commissioning a linear accelerator. *Medical Physics*, 39:569–572, 2012.

L. V. v. Dijk, L. V. d. Bosch, P. Aljabar, D. Peressutti, S. Both, R. Steenbakkers, J. A. Langendijk, M. J. Gooding, and C. L. Brouwer. Improving automatic delineation for head and neck organs at risk by deep learning contouring. *Radiotherapy and Oncology*, 142:115–123, 2020. doi: 10.1016/j.radonc.2019.09.022.

Paul J. Doolan et al. A clinical evaluation of the performance of five commercial artificial intelligence contouring systems for radiotherapy. *Frontiers in Oncology*, 13:1213068, Aug 2023. doi: 10.3389/fonc.2023.1213068.

M. Douglass. Can optical scanning technologies replace ctct for 3D printed

medical devices in radiation oncology? *Journal of Medical Radiation Sciences*, 69:139–142, 2022. doi: 10.1002/jmrs.579.

A. Duffton, W. Li, and E. Forde. The pivotal role of the therapeutic radiographer/radiation therapist in image-guided radiotherapy research and development. *Clinical Oncology*, 32(12):852–860, 2020. ISSN 0936-6555. doi: 10.1016/j.clon.2020.09.009. Image-Guided Radiotherapy.

S. Dufreneix, J. Bellec, S. Josset, and L. Vieillevigne. Field output factors for small fields: A large multicentre study. *Physica Medica*, 81:191–196, 2021.

Elekta Instruments AB, Stockholm, Sweden. Versa HD Linear Accelerator, 2024. URL `https://www.elekta.com/products/radiation-therapy/versa-hd/`.

M. Field, N. Hardcastle, M. Jameson, N. J. Aherne, and L. Holloway. Machine learning applications in radiation oncology. *Physics and Imaging in Radiation Oncology*, 19:13–24, 2021. doi: 10.1016/j.phro.2021.05.007.

Benedick Fraass, Karen Doppke, Margie Hunt, Gerald Kutcher, George Starkschall, Robin Stern, and Jake Van Dyke. American association of physicists in medicine radiation therapy committee task group 53: Quality assurance for clinical radiotherapy treatment planning. Technical Report 10, American Association of Physicists in Medicine, 1998.

James M. Galvin, Gary Ezzell, Avraham Eisbrauch, Cedric Yu, Brian Butler, Yukun Xiao, Irwin Rosen, Michael Sharpe, Lei Xing, and Ping Xia. Basic applications of multileaf collimators. *Medical Physics*, 22(4):485–491, 1995.

M. Granja, S. Correia, and L. Alves. Access to general practitioners during the second year of the COVID-19 pandemic in portugal: a nationwide survey of doctors. *BMC Primary Care*, 24, 2023. doi: 10.1186/s12875-023-01994-x.

Timothy P. Hanna, Will D. King, Stephane Thibodeau, Matthew Jalink, Gregory A. Paulin, Elizeth Harvey-Jones, Dylan E. O'Sullivan, Christopher M. Booth, Richard Sullivan, and Ajay Aggarwal. Mortality due to cancer treat-

ment delay: Systematic review and meta-analysis. *BMJ*, page m4087, Nov 2020. doi: 10.1136/bmj.m4087.

V. Hernandez, J. Sáez, A. Angerud, R. Cayez, C. Khamphan, D. Nguyen, L. Vieillevigne, and V. Feygelman. Dosimetric leaf gap and leaf trailing effect in a double-stacked multi-leaf collimator. *Medical Physics*, 48(5), 2021.

Y. Hillman, J. Kim, I. Chetty, and N. Wen. Refinement of MLC modeling improves commercial QA dosimetry system for SRS and SBRT patient-specific QA. *Medical Physics*, 45(4):1351–1359, 2018.

IAEA. Absorbed dose determination in external beam radiotherapy: An international code of practice for dosimetry based on standards of absorbed dose to water. Technical Reports Series No. 398. Technical report, International Atomic Energy Agency, Vienna, Austria, 2001.

IAEA. *Accuracy Requirements and Uncertainties in Radiotherapy*. International Atomic Energy Agency, Vienna, 2017.

N. Kakade, R. Kumar, S. Sharma, V. Mittal, and D. Datta. Pretreatment dose verification in volumetric modulated arc therapy using liquid ionization chamber. *Journal of Medical Physics*, 44:9 – 15, 2019. doi: 10.4103/JMP.JMP_108_18.

Pavel Kazantsev, Wolfgang Lechner, Eduard Gershkevitsh, Catharine H. Clark, Daniel Venencia, Jacob Van Dyk, Paulina Wesolowska, Victor Hernandez, Nuria Jornet, Milan Tomsej, Tomislav Bokulic, and Joanna Izewska. IAEA methodology for on-site end-to-end IMRT/VMAT audits: An international pilot study. *Acta Oncologica*, 59(2):141–148, 2020. doi: 10.1080/0284186X.2019.1685128.

Faiz M. Khan and John P. Gibbons. *Khan's The Physics of Radiation Therapy*. Wolters Kluwer, Philadelphia, 2020.

R. G. J. Kierkels, Victor Hernandez, J. Sáez, A. Angerud, G. C. Hilgers, Kathrin Surmann, Danny Schuring, and André W. Minken. Multileaf col-

limator characterization and modeling for a 1.5 T MRI-linac using static synchronous and asynchronous sweeping gaps. *Physics in Medicine & Biology*, 2024.

K. Kisling, L. Zhang, H. Simonds, N. Fakie, Jinzhong Yang, R. McCarroll, P. Balter, H. Burger, O. Bogler, R. Howell, K. Schmeler, M. Mejia, B. Beadle, A. Jhingran, and L. Court. Fully automatic treatment planning for external-beam radiation therapy of locally advanced cervical cancer: A tool for low-resource clinics. *Journal of Global Oncology*, 2019(5):1–12, 2019. doi: 10.1200/JGO.18.00107.

Kuniaki Kitagawa, Richard T George, Armin Arbab-Zadeh, Joao AC Lima, and Albert C Lardo. Characterization and correction of beam-hardening artifacts during dynamic volume ct assessment of myocardial perfusion. *Radiology*, 256(1):111–118, 2010. doi: 10.1148/radiol.10091399.

X. Kong, J. Harris, D. Spitznagel, and J. Walker. SU-E-T-312: Dosimetric consideration for the Agility MLC when planning rotational SRT/SBRT treatments. *Medical Physics*, 42:3405–3405, 2015. doi: 10.1118/1.4924673.

S. Korreman, J. G. Eriksen, and C. Grau. The changing role of radiation oncology professionals in a world of ai – just jobs lost – or a solution to the under-provision of radiotherapy? *Clinical and Translational Radiation Oncology*, 26:104–107, 2021. doi: 10.1016/j.ctro.2020.04.012.

Gerald J. Kutcher, Lawrence Coia, Michael Gillin, William F. Hanson, Steven Leibel, Ralph J. Morton, Jatinder R. Palta, James A. Purdy, Douglas R. Reeve, Gunnar K. Svensson, Mark Weller, and Lucille Wingfield. Comprehensive qa for radiation oncology: Report of aapm radiation therapy committee task group 40. Report TG 40, American Association of Physicists in Medicine, 1994.

Katja M. Langen, Nikos Papanikolaou, John Balog, Richard Crilly, David Followill, Shruti M. Goddu, William H. Grant, Rebecca M. Howell, Marc L. Kessler, Tony Kim, Karen L. Lam, Hua Li, Daniel A. Low, Thomas R.

Mackie, Kevin Mittauer, Jatinder Palta, Charles R. Ramsey, Jeff Shi, Timothy D. Solberg, Jack Venselaar, Kevin Woch, and Ping Xia. QA for helical tomotherapy: Report of the AAPM Task Group 148. *Medical Physics*, 37 (9):4817–4853, 2010. ISSN 0094-2405. doi: 10.1118/1.3462971.

Michael C. Lee, Jun Deng, Jinsheng Li, Steve B. Jiang, and C-M. Charlie Ma. Monte carlo based treatment planning for modulated electron beam radiation therapy. *Physics in Medicine and Biology*, 46(8):2177, 2001. doi: 10.1088/0031-9155/46/8/310.

R. Lim, G. P. Penoncello, D. Hobbis, D. P. Harrington, and Y. Rong. Technical Note: Characterization Of Novel Iterative reconstructed cone beam CT images for dose tracking and adaptive radiotherapy on l-shape linacs. *Medical Physics*, 49:7715–7732, 2022.

D. Létourneau, J. Publicover, J. Kozelka, D. J. Moseley, and D. A. Jaffray. Novel dose verification method for VMAT treatment delivery. *Medical Physics*, 36(12):5535–5541, 2009. doi: 10.1118/1.3253464.

L. B. Marks, R. D. Adams, T. Pawlicki, A. L. Blumberg, D. Hoopes, M. Brundage, and B. A. Fraass. Enhancing the role of case-oriented peer review to improve quality and safety in radiation oncology: executive summary. *Practical Radiation Oncology*, 3:149–156, 2013. doi: 10.1016/j.prro.2012.11.010.

Philip Mayles, Alan E. Nahum, and Jean-Claude Rosenwald. *Handbook of Radiotherapy Physics: Theory and Practice*. CRC Press/Taylor and Francis Group, Boca Raton, FL, 2022.

A. McWilliam, W. Beasley, and C. Rowbottom. Relationship between geometric and dosimetric accuracy of auto-contouring in head and neck VMAT treatment planning. *Radiotherapy and Oncology*, 115(Supplement 1):S530, 2015. doi: 10.1016/S0167-8140(15)40928-4.

Philippe Meyer, Vincent Noblet, Clément Mazzara, and Alex Lallement. Sur-

vey on deep learning for radiotherapy. *Computers in Biology and Medicine*, 98:126–146, 2018. doi: 10.1016/j.compbiomed.2018.05.018.

Moyed Miften, Arthur Olch, Dimitris Mihailidis, Jean Moran, Todd Pawlicki, Andrea Molineu, Harold Li, Krishni Wijesooriya, Jie Shi, Ping Xia, Nikos Papanikolaou, and Daniel A. Low. Tolerance limits and methodologies for imrt measurement-based verification QA: Recommendations of AAPM Task Group No. 218. *Medical Physics*, 45(4):e53–e83, 2018. doi: 10.1002/mp.12810.

Glenford J. Myers, Corey Sandler, and Tom Badgett. *The Art of Software Testing*. John Wiley & Sons, 2012.

Ganesh Narayanasamy, Daniel L. Saenz, Dewayne Defoor, Niko Papanikolaou, and Sotirios Stathakis. Dosimetric validation of Monaco treatment planning system on an Elekta Versa HD linear accelerator. *Journal of Applied Clinical Medical Physics*, 18(6):123–129, 2017.

T. Netherton, Y. Li, S. Gao, A. Klopp, P. Balter, L. Court, R. Scheuermann, C. Kennedy, L. Dong, J. Metz, D. Mihailidis, C. Ling, M. Lee, M. Constantin, S. Thompson, J. Kauppinen, and P. Uusitalo. Experience In Commissioning the Halcyon Linac. *Medical Physics*, 46:4304–4313, 2019.

Dag Rune Olsen, Øyvind S Bruland, and Brian J Davis. Telemedicine in radiotherapy treatment planning: requirements and applications. *Radiotherapy and Oncology*, 54(3):255–259, 2000. ISSN 0167-8140. doi: https://doi.org/10.1016/S0167-8140(99)00185-1. URL `https://www.sciencedirect.com/science/article/pii/S0167814099001851`.

K. F. Otto. Volumetric modulated arc therapy: IMRT in a single gantry arc. *Medical Physics*, 35:310–317, 2007. doi: 10.1118/1.2818738.

H. Palmans, P. Andreo, M. S. Huq, J. Seuntjens, K. E. Christaki, and A. Meghzifene. Dosimetry of small static fields used in external photon beam radiotherapy: Summary of TRS-483, the IAEA-AAPM international

code of practice for reference and relative dose determination. Technical Report 483, International Atomic Energy Agency, 2018.

C. Papoutsi, S. Shaw, and T. Greenhalgh. Implementing video group consultations in general practice during COVID-19: a qualitative study. *British Journal of General Practice*, 72:e483–e491, 2022. doi: 10.3399/bjgp.2021.0673.

J. Park, Q. Xu, J. Xue, Y. Zhai, L. An, and Y. Chen. SU-E-T-119: Dosimetric and Mechanical Characteristics of Elekta Infinity Linac with Agility MLC. *Medical Physics*, 41(6):249, 2014. doi: 10.1118/1.4888449.

D. Pasalic, J. P. Reddy, T. Edwards, H. Y. Pan, and B. D. Smith. Implementing an electronic data capture system to improve clinical workflow in a large academic radiation oncology practice. *JCO Clinical Cancer Informatics*, pages 1–12, 2018. doi: 10.1200/cci.18.00034.

Todd Pawlicki, Peter Dunscombe, Arno Mundt, and Pierre Scalliet. *Quality and Safety in Radiotherapy*. CRC Press, 2011.

Boyd L. Perry. Effective methods for software and systems integration. *Auerbach Publications*, 2009.

PTW Freiburg. *Detectors for Ionizing Radiation*, 2024. URL `https://www.ptwdosimetry.com/`. Accessed: 2023-08-22.

B. W. Raaymakers, I. M. Jürgenliemk-Schulz, G. H. Bol, M. Glitzner, A. Kotte, B. v. Asselen, J. d. Boer, J. Bluemink, S. Hackett, M. A. Moerland, S. Woodings, J. Wolthaus, H. M. v. Zijp, M. Philippens, R. H. N. Tijssen, J. G. M. Kok, E. N. d. G. Breugel, I. Kiekebosch, L. Meijers, C. Nomden, G. Sikkes, P. Doornaert, W. S. Eppinga, N. Kasperts, L. G. Kerkmeijer, J. Tersteeg, K. J. Brown, B. Pais, P. Woodhead, and J. J. W. Lagendijk. First patients treated with a 1.5 T MRI-Linac: clinical proof of concept of a high-precision, high-field mri guided radiotherapy treatment. *Physics in Medicine and Biology*, 62:L41–L50, 2017. doi: 10.1088/1361-6560/aa9517.

Republic of South Africa. Protection of Personal Information Act, 2013, 2013.

URL https://www.gov.za/documents/protection-personal-information-act-26-nov-2013-0000. Government Gazette, No. 37067, Vol. 581, Cape Town, 26 November 2013.

D. J. Rhee, A. Jhingran, B. Rigaud, T. Netherton, C. Cárdenas, L. Zhang, S. Vedam, S. F. Kry, K. K. Brock, W. V. Shaw, F. O'Reilly, J. Parkes, H. Burger, N. Fakie, C. Trauernicht, H. Simonds, and L. E. Court. Automatic contouring system for cervical cancer using convolutional neural networks. *Medical Physics*, 47:5648–5658, 2020. doi: 10.1002/mp.14467.

A. V. d. Schoot, W. V. D. Wollenberg, C. Carbaat, P. d. Ruiter, M. E. Nowee, F. J. Pos, B. v. Triest, J. Sonke, and T. Janssen. Evaluation of plan quality in radiotherapy planning with an MR-Linac. *Physics and Imaging in Radiation Oncology*, 10:19–24, 2019. doi: 10.1016/j.phro.2019.04.004.

J. Shen, Y. Tao, H. Guan, H. Zhen, L. He, T. Dong, S. Wang, Y. Chen, C. Qi, Z. Liu, and F. Zhang. Clinical validation and treatment plan evaluation based on auto-delineation of the clinical target volume for prostate cancer radiotherapy. *Research Square*, 2022. doi: 10.21203/rs.3.rs-1226468/v1.

Siemens Healthineers. *AI-Rad Companion*, 2023. URL https://www.siemens-healthineers.com/en-za/digital-health-solutions/ai-rad-companion. Accessed: 2023-12-12.

G. Smyth, J. C. Bamber, P. Evans, and J. L. Bedford. Trajectory optimization for dynamic couch rotation during volumetric modulated arc radiotherapy. *Physics in Medicine and Biology*, 58:8163–8177, 2013. doi: 10.1088/0031-9155/58/22/8163.

Christopher M. Thompson, Stuart J. Weston, Vincent C. Cosgrove, and David I. Thwaites. A dosimetric characterization of a novel linear accelerator collimator. *Medical Physics*, 41(3):031713, 2014. doi: 10.1118/1.4866228. URL https://doi.org/10.1118/1.4866228.

Naoki Tohyama, Hiroyuki Okamoto, Kohei Shimomura, Masahiko Kurooka, Ryu Kawamorita, Seiichi Ota, Toru Kojima, Naoki Hayashi, Masahiko Oku-

mura, Masaru Nakamura, Mitsuhiro Nakamura, Atsushi Myojoyama, and Hiroshi Onishi. A national survey on the medical physics workload of external beam radiotherapy in Japan†. *Journal of Radiation Research*, 64 (6):911–925, 10 2023. ISSN 1349-9157. doi: 10.1093/jrr/rrad070. URL https://doi.org/10.1093/jrr/rrad070.

Ghada Trabelsi, Philippe Leray, Mounir Ben Ayed, and Adel M. Alimi. Benchmarking dynamic bayesian network structure learning algorithms. *IEEE*, pages 1–6, 2013. doi: 10.1109/ICMSAO.2013.6552549.

A. Van Esch, L. Tillikainen, J. Pyykkonen, M. Tenhunen, H. Helminen, S. Siljamäki, J. Alakuijala, M. Paiusco, M. Iori, and D. Huyskens. Testing of the analytical anisotropic algorithm for photon dose calculation. *Medical Physics*, 33(11):4130–4148, 2006. doi: 10.1118/1.2358333. URL https://consensus.app/papers/testing-anisotropic-algorithm-photon-dose-calculation-esch/0b0aafedd1ea59e797ce7bac8ab77fdd/?utm_source=chatgpt.

Varian Medical Systems, Palo Alto, CA. *Eclipse Photon and Electron Algorithms Reference Guide*. Eclipse Foundation, Ottawa, Canada, 1st edition, 2018.

Varian Medical Systems, Palo Alto, CA. Eclipse treatment planning system, 2024. URL https://www.varian.com/products/radiotherapy/treatment-planning/eclipse.

Jack Venselaar and Hans Welleweerd. Application of a test package in an intercomparison of the photon dose calculation performance of treatment planning systems used in a clinical setting. *Radiotherapy and Oncology*, 60 (2):203–213, 2001.

Charles M. Washington and Dennis T. Leaver. *Principles and Practice of Radiation Therapy*. Elsevier Health Sciences, 2015.

J. Wong, V. Huang, D. Wells, J. Giambattista, C. Kolbeck, K. F. Otto, E. P. Saibishkumar, and A. Alexander. Implementation of deep learning-based

auto-segmentation for radiotherapy planning structures: a workflow study at two cancer centers. *Radiation Oncology*, 16, 2021. doi: 10.1186/s13014-021-01831-4.

Zhengzheng Xu, Gregory Warrell, Soyoung Lee, Valdir C. Colussi, Y. Zheng, Rodney J. Ellis, Mitchell Machtay, and Tarun Podder. Assessment of beam-matched Linacs quality/accuracy for interchanging SBRT or SRT patient using VMAT without replanning. *Journal of Applied Clinical Medical Physics*, 20(1):68–75, 2019. doi: 10.1002/acm2.12492.

Di Yan, Frank Vicini, John Wong, and Alvaro Martinez. Adaptive radiation therapy: Predicting and assessing changes in tumor anatomy. *Medical Physics*, 24(10):1595–1606, 1997. doi: 10.1118/1.597672.

J. Yang, Jinsheng Li, Ling Qin, W. Xiong, and C. Ma. Modelling of electron contamination in clinical photon beams for monte carlo dose calculation. *Physics in Medicine and Biology*, 49(12):2657–2673, 2004. doi: 10.1088/0031-9155/49/12/013. URL `https://consensus.app/papers/modelling-electron-contamination-photon-beams-monte-yang/e4367317a86d5af6b742f6a1afce884c/?utm_source=chatgpt`.

W. Yao and J. Farr. Determining the optimal dosimetric leaf gap setting for rounded leaf-end multileaf collimator systems by simple test fields. *Journal of Applied Clinical Medical Physics*, 16(4), 2015.

L. Yu, T. L. S. Tang, N. Cassim, A. G. Livingstone, D. Cassidy, T. Kairn, and S. Crowe. Analysis of dose comparison techniques for patient-specific quality assurance in radiation therapy. *Journal of Applied Clinical Medical Physics*, 20:189–198, 2019. doi: 10.1002/acm2.12726.

W. J. Zabel, J. L. Conway, A. Gladwish, J. Skliarenko, G. DiDiodato, L. Goorts-Matthews, A. Michalak, S. Reistetter, J. King, K. Nakonechny, K. Malkoske, M. N. Tran, and N. McVicar. Clinical evaluation of deep learning and atlas-based auto-contouring of bladder and rectum for prostate

radiation therapy. *Practical Radiation Oncology*, 11:e80–e89, 2021. doi: 10.1016/j.prro.2020.05.013.

You Zhang, Anh H. Le, Zhen Tian, Zohaib Iqbal, Tsuicheng Chiu, Xuejun Gu, Andrei Pugachev, Robert Reynolds, Yang K. Park, Mu-Han Lin, and Strahinja Stojadinovic. Modeling elekta versa hd using the varian eclipse treatment planning system for photon beams: A single-institution experience. *Journal of Applied Clinical Medical Physics*, 20(10):33–42, 2019.